DSIAC JOURNAL

A Quarterly Publication of the Defense Systems Information Analysis Center

Volume 6 • Number 4 • Fall 2019

EFFECTS

of Material Properties on ISR for Synthetic Aperture Radar

DSIAC JOURNAL

VOLUME 6 | NUMBER 4 | FALL 2019

Editor-in-Chief: Brian Benesch
Copy Editor: Maria Brady
Art Director: Melissa Gestido

On the Cover:
(Source: 123rf.com)

The *DSIAC Journal* is a quarterly publication of the Defense Systems Information Analysis Center (DSIAC). DSIAC is a DoD Information Analysis Center (IAC) sponsored by the Defense Technical Information Center (DTIC) with policy oversight provided by the Office of the Under Secretary of Defense (OUSD) for Research and Engineering (R&E). DSIAC is operated by the SURVICE Engineering Company with support from Georgia Tech Research Institute, Texas Research Institute/Austin, and The Johns Hopkins University.

Distribution Statement A: Approved for public release; distribution is unlimited.

ISSN 2471-3392 *(Print)*
ISSN 2471-3406 *(Online)*

Focus Area Key:

AM *Advanced Materials*	EN *Energetics*	RQ *RMQSI*
AS *Autonomous Systems*	MS *Military Systems*	SV *Survivability & Vulnerability*
DE *Directed Energy*	NW *Non-lethal Weapons*	WS *Weapon Systems*

ABOUT DSIAC

PURPOSE

The purpose of DSIAC is to provide information research and analysis for DoD and federal government users to stimulate innovation, foster collaboration, and eliminate redundancy.

MISSION

The mission of DSIAC is to generate, collect, analyze, synthesize, and disseminate scientific and technical information (STI) to DoD and federal government users and industry contractors.

VISION

DSIAC will be the premier information research partner and curator of technology advancements and trends for the defense systems community.

PRODUCTS & SERVICES

TECHNICAL INQUIRIES (TIs)

We offer 4 hours of information research (free to the client) in response to TIs on any of the DSIAC subject areas. TI response efforts generally include literature searches, document requests, answers to technical questions, and expert referrals.

CORE ANALYSIS TASKS (CATs)

We conduct customer-funded CATs that expand the limits of the free TI service. Each CAT is limited to a $1M ceiling and can be incrementally funded.

STI UPLOAD

We collect STI, adding it to the DTIC collection, and ensuring that the body of information is available to share with the DoD community.

TRAINING/EVENTS

We participate, host, and promote key technical conferences and forums to engage and network with the science and technology (S&T) community.

PROMOTION

We publicize events, technologies, information research products, and more to our +75,000 members.

INFORMATION RESEARCH PRODUCTS

We publish the DSIAC Journal, Defense Systems Digest, State-of-the-Art Reports (SOARs), and many other information products available for free electronic download on our website.

HOW TO CONTACT DSIAC

Ted Welsh
DSIAC Director

Brian Benesch
DSIAC Technical Project Lead

DSIAC HEADQUARTERS

4695 Millennium Drive
Belcamp, MD 21017-1505
Office: 443.360.4600
Fax: 410.272.6763
Email: contact@dsiac.org ▸

WPAFB SATELLITE OFFICE

704 TG/OL-AC/DSIAC
2700 D Street, Building 1661
Wright-Patterson AFB, OH 45433-7403
Office: 937.255.3828
DSN: 785.3828
Fax: 937.255.9673

DSIAC CONTRACTING OFFICER REPRESENTATIVE

Peggy M. Wagner (COR)
704 TG/OL-AC
2700 D Street, Building 1661
Wright-Patterson AFB, OH 45433-7403
Office: 937.255.6302

DSIAC PROGRAM MANAGEMENT ANALYST

Emese Horvath
IAC Program Management Office (DTIC-I)
8725 John J. Kingman Road
Fort Belvoir, VA 22060
Office: 571.448.9753

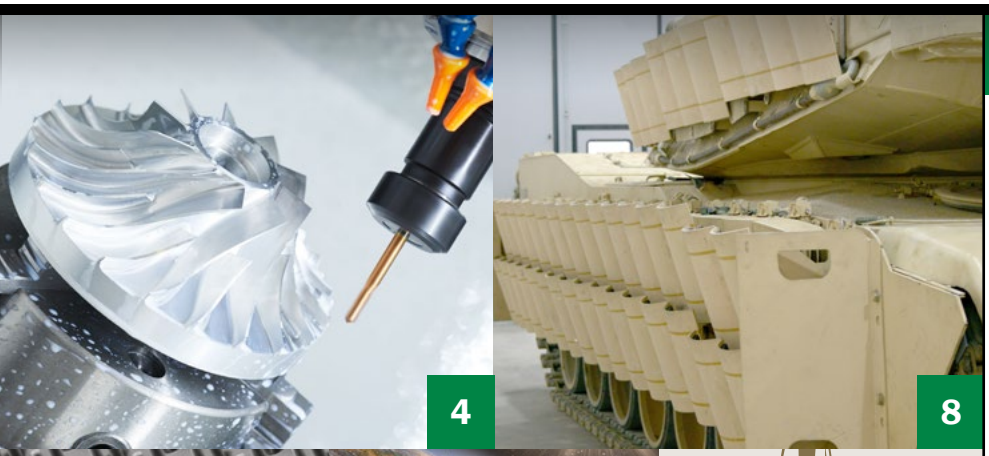

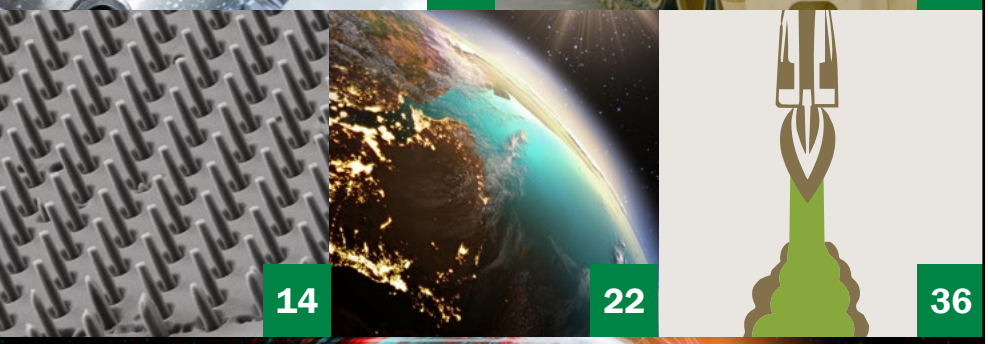

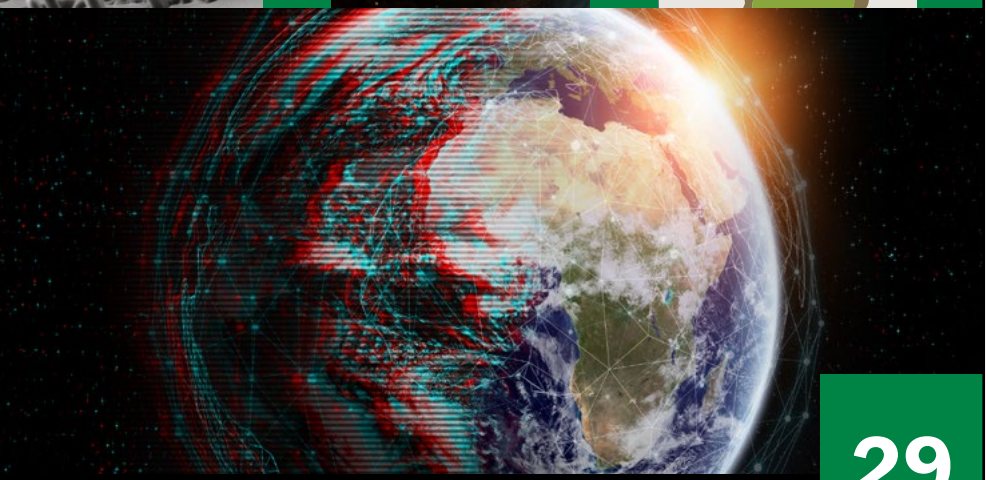

FEATURE

Effects of Material Properties on ISR for Synthetic Aperture Radar

By Qaisar Manzoor
MS *Military Sensing*

This research looks at the various factors that affect image appearance of a target in microwave and radar frequencies. To better understand how to implement unconventional countermeasures, it is important to understand the physical and material properties that affect target detection, recognition, and identification in intelligence, surveillance, and reconnaissance (ISR) missions.

CONTENTS

High-Strength, Corrosion-Resistant

STEEL OVER TITANIUM ALLOY

for Aircraft Critical Components

By Gregory Vartanov

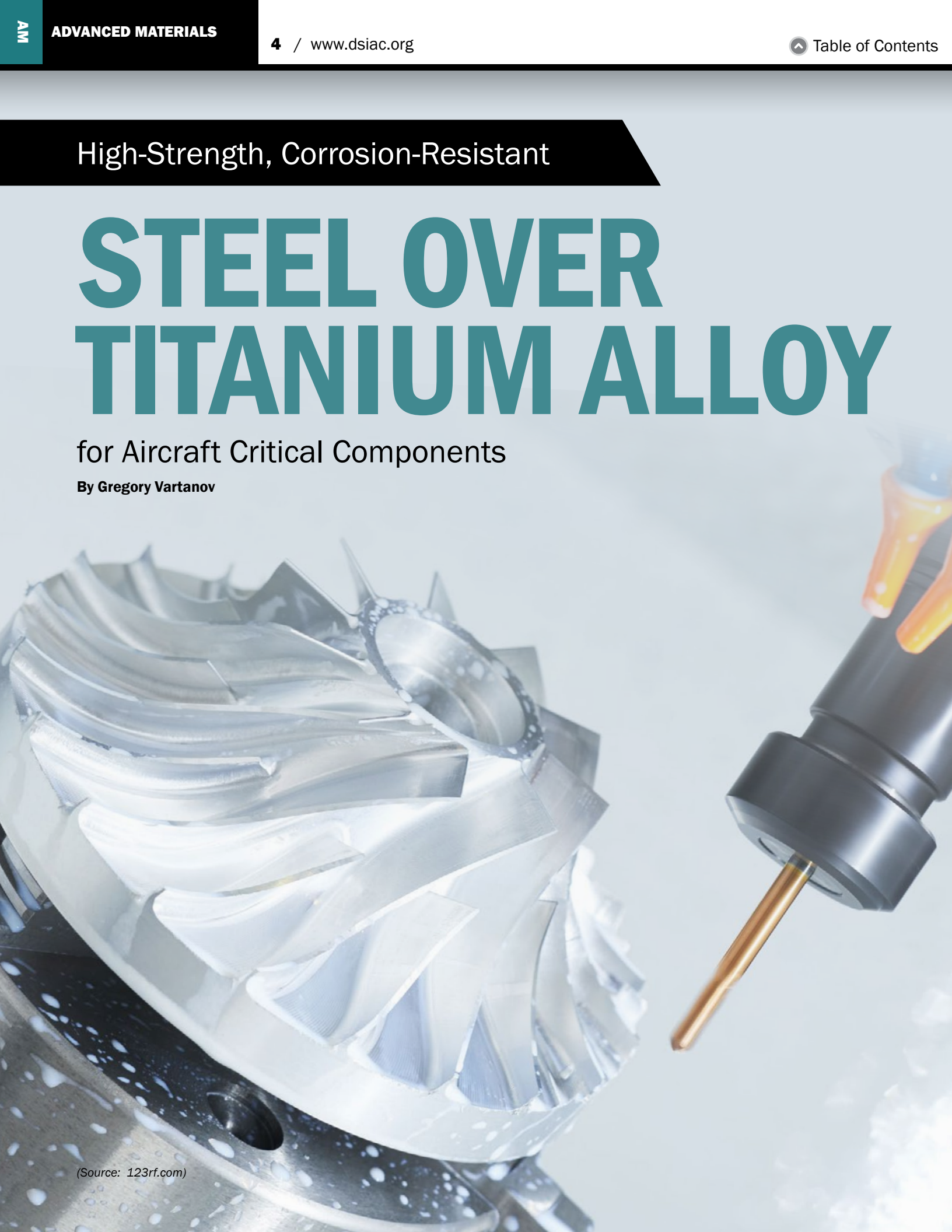

(Source: 123rf.com)

INTRODUCTION

Aircraft landing gears, structures, and turbine components ("aircraft critical components") are subjected to severe loading, corrosion, and adverse environmental conditions and have complex shapes varying from thin to thick sections. High-strength titanium alloys and steels are widely used for aircraft critical, high-stressed components. These materials are chosen because of their specific strength, tensile strength-to-density ratio, and fatigue strength and toughness.

High-strength titanium alloys such as Ti-6Al-4V, Ti-10V-2Fe-3Al, and Ti-5Al-2Sn-2Zr-4Cr-4Mo are excellent candidates for aircraft landing gears and structures due to their high specific and fatigue strengths, good toughness, and excellent corrosion resistance. However, high cost limits their applications.

This article proposes quenched and tempered high-strength, corrosion-resistant (HSCR) steel as a suitable replacement for manufacturing aircraft critical, high-stressed components due to its high specific and fatigue strengths, good toughness, and corrosion resistance [1].

DESCRIPTION

HSCR (i.e., stainless) steel and high-strength titanium alloy are two options for critical high-stressed aircraft landing gears and structures. These two materials have their advantages and shortcomings.

METHODS AND PROCESSES

Premium-quality HSCR steel ingots are produced by vacuum melting processes. HSCR steel powder can be produced by atomization processes, including vacuum atomization.

High-strength titanium alloys and steels are widely used for aircraft critical, high-stressed components.

Aircraft critical components can be manufactured from the HSCR steel or high-strength titanium alloy by the following three methods:

1. Hot working (HW) – hot working the melted ingots, including forging, rolling, and pressing, followed by machining and hardening.
2. Powder metallurgically-based, hot isostatic pressing (PM HIP) – hot isostatic pressing of powder followed by machining and hardening.
3. Additive manufacturing (AM) – additive manufacturing powder followed by finish machining and heat treatment.

HSCR steel hardening consists of austenitizing and rapid cooling, optional refrigeration, and tempering at low, medium, and high temperatures (secondary hardening) that depend on the required properties.

MANUFACTURING THE COMPONENTS

Formation of near net shape (NNS) by PM HIP allows manufacturing various types of the complex-shaped, aircraft critical components [2]. The process supplies precise geometry of the articles and properties close to the forgings. PM HIP article cost is generally higher than the cost of HW articles; however, small batches of the large-section articles are economically feasible to produce by PM HIP rather than HW of the melted ingots. Figure 1 shows an example NNS part made by PM HIP.

Manufacturing the aircraft components by PM HIP from the HSCR steel powder achieves a higher quality at a reasonable cost. Components made by PM HIP from the HSCR steel powder have the same lifetime and durability at lower cost than the same weight components made by

Figure 1: Impeller for Turbo Pump Made by PM HIP From Ti-6Al-4V Alloy *(Source: LNT PM Inc.).*

PM HIP from high-strength titanium alloy powder.

AM allows manufacturing NNS articles of high-strength titanium alloys. The NNS article made by AM is cost-effective due to minimizing waste. The "buy-to-fly" ratio (the ratio of the mass of raw material to the mass of the product) is significantly lower than the hot-worked articles. However, extremely high costs of titanium powder and manufacturing, high oxidation, and issues with heat treatment and machining limit AM of titanium alloys.

Aircraft critical components made by AM from the HSCR steel powder are a lower cost alternative to the same weight components made by AM from the titanium alloy powder.

COMPARING PROPERTIES

Table 1 shows the room-temperature mechanical properties of samples of the HSCR steel and Ti-6Al-4V alloy made by the following three different processes:

> Manufacturing the aircraft components by PM HIP from the HSCR steel powder achieves a higher quality at a reasonable cost.

1. HW + hardening – hot-worked HSCR steel hardened by quenching, refrigerating, and tempering (QRT) and the hot-worked Ti-6-4 alloy hardened by solution treating and aging (STA) [3].
2. PM HIP + hardening – consolidated by HIP of HSCR steel powder hardened by QRT and the Ti-6-4 alloy powder hardened by STA.
3. Selective laser melting (SLM) + annealing – built with the SLM using the HSCR steel powder, followed by annealing and the built-by SLM using the Ti-6-4 alloy powder [4].

Figure 2 shows the comparison of the mechanical properties. In the figure, HSCR steel made by three different processes has slightly higher E/ρ and UTS/ρ, higher S, the same $K_{1C,}$ and higher CVN than the Ti-6-4 alloy manufactured by the same processes. Also, the HSCR steel has higher elevated temperature strength, better workability and machinability, and better wear resistance, although the Ti-6-4 alloy has better corrosion resistance.

Given the superior material properties of the HSCR over the Ti-6Al-4V aircraft critical components manufactured by HW, PM HIP, and SLM processes, the Ti-6Al-4V alloy can be substituted with the same weight aircraft components, manufactured by the same processes from the HSCR steel, and without sacrificing stiffness, durability, and lifetime.

The aircraft components manufactured by HW, PM HIP, and SLM processes have at least 25% projected cost reductions compared to the same weight components from the Ti-6Al-4V alloy.

Table 1: Mechanical Properties of the HSCR Steel and Ti-6Al-4V Alloy

PROCESSES	HW + HARDENING		PM HIP+ HARDENING		SLM + ANNEALING	
Materials	HSCR	Ti-6-4	HSCR	Ti-6-4	HSCR	Ti-6-4
Density (ρ), lb/in³	0.280	0.160	0.280	0.160	0.280	0.160
Modulus Elasticity (E), ksi	31160	16670	31160	16670	31160	16670
Specific Stiffness (E/ρ)	**111280**	**104160**	**111280**	**104160**	**111280**	**104160**
Tensile Strength (UTS), ksi	294	165	290	159	291	162
Specific Strength (UTS/ρ)	**1050**	**1030**	**1037**	**994**	**1039**	**1013**
Yield Strength (YS), ksi	226	151	220	145	223	148
Fatigue Limits (S) at 10^7 Cycles, ksi	120	100	116	90	117	90
Elongation (El), %	10	10	10	9	10	10
Reduction of Area (RA), %	36	34	40	30	34	30
Fracture Toughness (K_{1C}), ksi√in	65	70	70	75	60	65
Charpy V-Notch Impact Toughness Energy (CVN), ft-lb	22	16	20	14	20	14

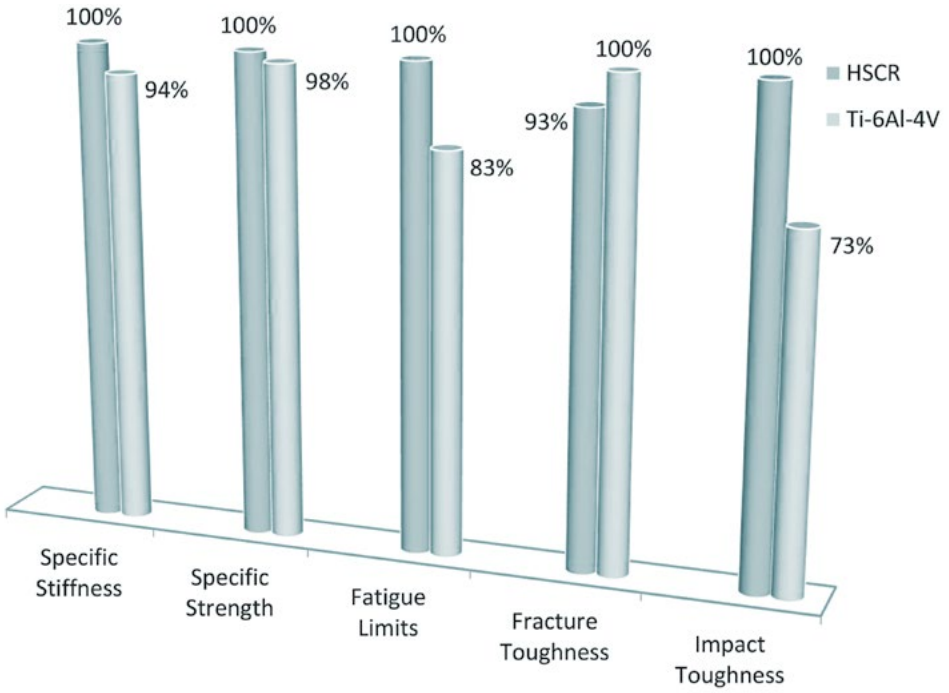

Figure 2: Summary of Comparing Key Properties of HSCR Steel and Ti-6Al-4V Alloy *(Source: Table 1).*

LNT PM Inc. is planning a pilot production for the NNS, aircraft critical components made from HSCR steel powder by PM HIP as a lower cost substitution of the high-strength titanium alloys. The HSCR steel is suited for defense industry applications such as missiles, artillery barrels, military land vehicles, and other applications, wherein high-strength and fatigue limits, good toughness, and corrosion resistance at reasonable cost are required.

CONCLUSIONS

HSCR steel possesses a specific strength that is slightly higher than the Ti-6Al-4V alloy at the same toughness. Therefore, HSCR steel can be substituted for the Ti-6Al-4V alloy in manufacturing aircraft critical components.

Projected cost of manufacturing the aircraft critical components from the corrosion-resistant steel is significantly lower than the Ti-6Al-4V alloy.

Additionally, manufacturing the aircraft critical components made from the HSCR steel reduces the energy consumption by 25% or more compared to the Ti-6Al-4V alloy. Using HSCR steel reduces the aircraft manufacturers' dependency of titanium from the monopoly of suppliers on the world market. ■

Manufacturing the aircraft critical components made from the HSCR steel reduces the energy consumption by 25% or more.

REFERENCES

[1] Vartanov, G. "High Strength CRA Ideal for Landing Gear." *Stainless Steel World*, vol. 29, p. 42, April 2017.

[2] Samarov, V., D. Seliverstov, and F. H. (Sam) Froes. "Fabrication of Near-Net Shape Cost-Effective Titanium Components by Use of Prealloyed Powder and Hot Isostatic Pressing." *ASM Handbook*, vol. 7: Powder Metallurgy, pp. 660–670, 2015.

[3] Carpenter Technology Corp. "Titanium Alloy Ti-6Al-4V." Technical datasheet, https://cartech.ides.com/datasheet.aspx?i=101&E=268, 1 July 2000.

[4] Liu, S., and Y. C. Shin. "Additive Manufacturing of Ti6Al4V Alloy: A Review." *Materials and Design*, vol. 164, no. 107552, 2019.

BIOGRAPHY

GREGORY VARTANOV is the chief engineer of Advanced Materials Development Corp., a Toronto-based company that develops high-strength steels and alloys focusing on aerospace and defense applications. His interests include developing high-strength steels, alloys, and composites, as well as designing critical components for aerospace and defense applications. He has five U.S. patents and more than 10 publications in high-strength steels and alloys. Dr. Vartanov holds an M.S. and Ph.D. in materials science and metallurgy.

VEHICLE PROTECTION:

Underpinning Advanced Armor Research and Impact on Survivability

By Valerie Wagoner

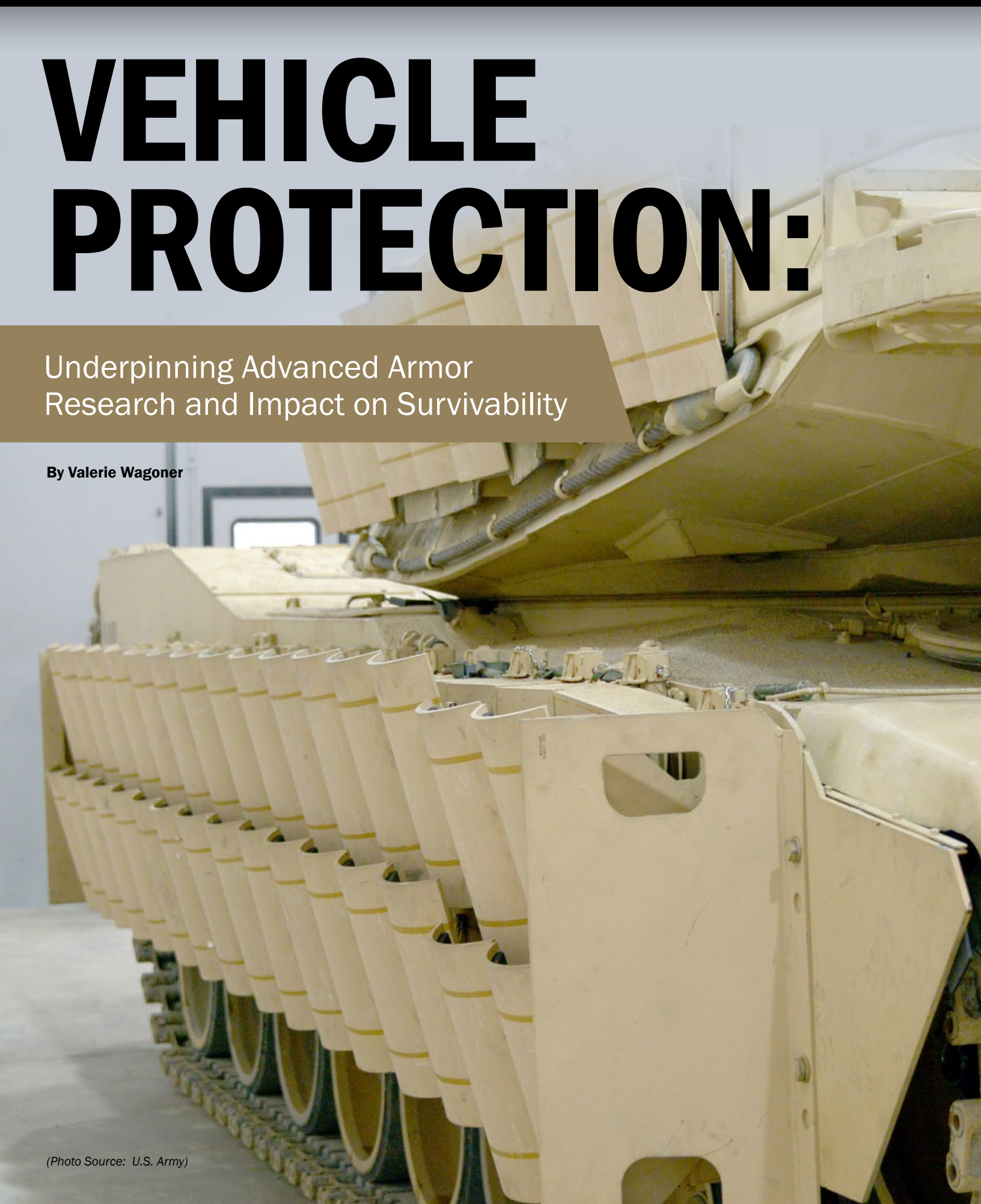

(Photo Source: U.S. Army)

BACKGROUND

The U.S. Army Futures Command (AFC) has been established to lead the Army's future force modernization enterprise. Within AFC, the U.S. Army Research Laboratory (ARL) has transitioned into the U.S. Army Combat Capabilities Development Command (CCDC). With this shift, ARL's role as the Army's corporate research laboratory has a reemphasized focus on discovery, innovation, and transition of science and technology (S&T) developments for future multidomain operations [1].

INTRODUCTION

As an Army leader in protection research and development (R&D), ARL performs high-impact foundational research that is disruptive and unique to the Army [1]. ARL researchers are continually improving the understanding of scientific fundamentals and innovating advanced protection mechanisms for mass-efficient ballistics and blast protection technologies to defeat the full range of conventional and projected antiarmor threats for Army and other agency platforms and personnel.

> Protection sciences has had significant and consistent impact on the Army for decades.

Protection sciences, one of the seven ARL core technical competencies shown in Figure 1 [1], has had significant and consistent impact on the Army for decades. ARL collaborative R&D efforts with other U.S. Department of Defense (DoD) organizations, international partners, and cooperative research and development agreements (CRADAs) with industry have successfully led to producing and fielding superior protection technologies to improve survivability. Such platforms as the Abrams; Bradley; Stryker; Paladin; high-mobility, multipurpose, wheeled vehicle (HMMWV); route clearance fleet of vehicles; mine-resistant, ambush-protected (MRAP) family of vehicles; and the Army's newest combat platform, the armored multipurpose vehicle, are armored with multithreat protection technologies conceptualized and matured to Technology Readiness Level (TRL) 4 at ARL.

ARL is the nation's premier organization for survivability technology innovation. As shown in Figures 2 and 3, examples of fielded armor technology developed and transitioned by ARL over the years include the M60 reactive armor tile (the first U.S. reactive armor), Abrams side and frontal armors, and the Abrams reactive armor tile, as well as quick-reaction improvised explosive device (IED) and IED-explosively formed penetrator (EFP) armor kits for tactical wheeled vehicles in Operation Iraqi Freedom and Operation Enduring Freedom.

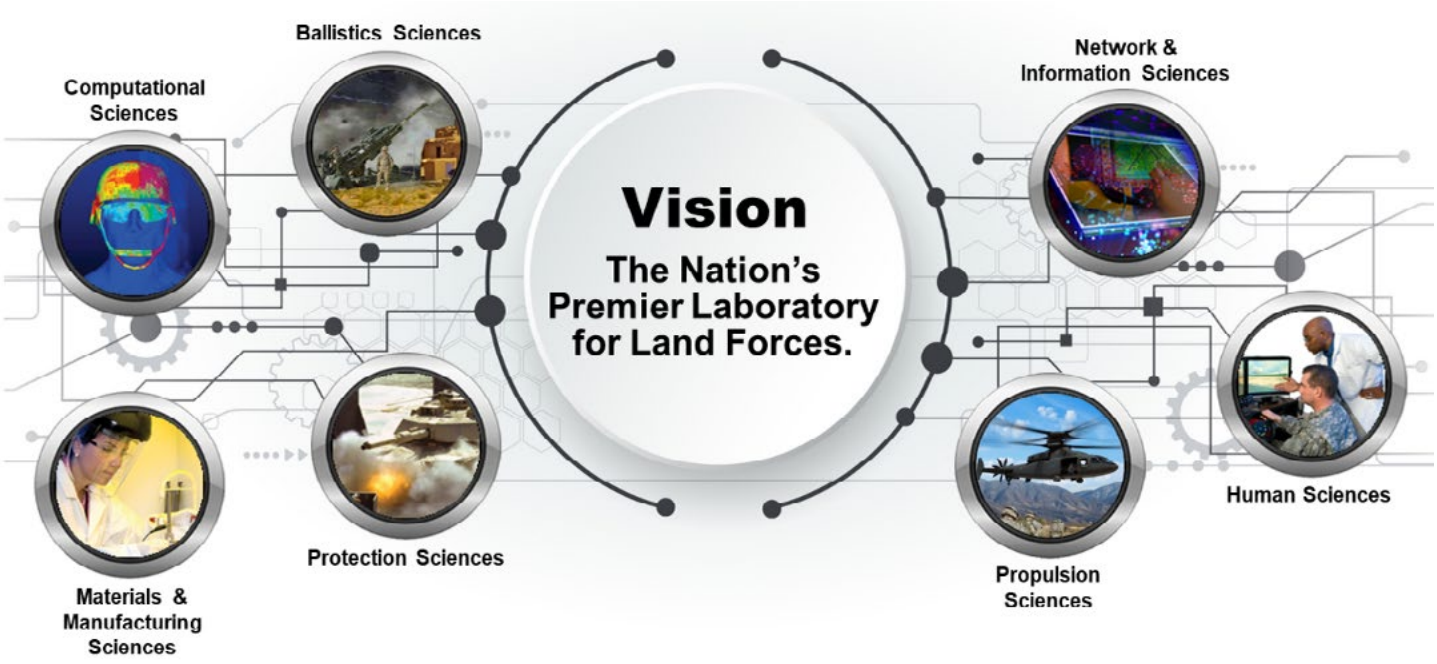

Figure 1: ARL's Core Technical Competencies *(Photo Courtesy of ARL).*

Figure 2: Reactive Armor Modules Containing ARL-Developed Technology Deployed on the Marine Corps' M60s Used in Desert Storm (Left) and the Abrams (Middle and Right) *(Photos Courtesy of ARL and GDLS/PM Abrams).*

Figure 3: Tactical Wheeled Vehicles With ARL-Designed Internal IED-EFP Armor Configurations: HMMWV M1114 (Left), RG33 (Middle), and MaxxPro MRAP (Right) [3] *(Photos Courtesy of ARL, ATC, and PM MRAP).*

Protection R&D for Future Readiness

A wide variety of R&D is being conducted at the laboratory to provide robust protection capabilities from contemporary, emerging, and future battlefield threats that will enable freedom of maneuver across multidomain operations and ensure Army dominance in its operational environment [2]. These threats of interest include rocket-propelled grenades (RPGs), antitank guided missiles, direct-fire cannon threats, antitank mines, top-attack munitions, and IEDs.

ARL engineers and scientists are performing research to answer difficult survivability S&T questions in support of U.S. Army modernization. For example, research is being conducted to address the critical protection technology question: Can we identify, develop, and demonstrate technology related to threat sensing, rapid countermeasure selection, deployment (e.g., unmanned aerial vehicle [UAV] response), threat engagement, and system self-adaptation to evolving threats? [1].

ARL researchers are addressing this question through several R&D programs investigating multilayered systems that incorporate synergistic protection and lethality mechanisms; advanced passive, reactive, and electromagnetic armors, multipurpose UAVs, and responsive transparent armor; and adaptation of protection systems in time and space to defeat pacing threats [1].

After developing and demonstrating technology capability via high-performance computing (HPC) modeling and simulation (M&S)-driven ballistic experiments (TRL-4), ARL researchers transition the technologies to partners such as the CCDC Ground Vehicle Systems Center, program managers, and/or U.S. defense contractors for further engineering and integration. Knowledge gained through these cutting-edge research efforts will be critical for maintaining battlefield superiority to 2030 and beyond.

Unique Infrastructure: HPC Experimental Capabilities

ARL has the unique infrastructure and resources to conceive, grow, and preserve Army essential core technical survivability competencies. A variety of laboratories and unique facilities, such as the ARL DoD Supercomputing Resource Center (ARL DSRC) for HPC (shown in Figure 4), are located at Aberdeen Proving Ground (APG), MD [3, 4]. Scientists and engineers use these facilities to perform a wide

Figure 4: ARL DSRC *(Photo Courtesy of ARL).*

variety of innovative research, including ballistics and materials research. These facilities and capabilities also support collaborative research with other government organizations, industry, and academia.

> Knowledge gained through these cutting-edge research efforts will be critical for maintaining battlefield superiority to 2030 and beyond.

Protection research efforts span the continuum from basic research that improves the understanding of scientific ballistics phenomena to applied research that supports protection system technology developments and fielded system upgrades. Protection research areas of interest include novel armor materials explosives; penetration mechanics; multithreat armor mechanisms; energetics response and mitigation; physics phenomenology, high-rate material deformation and failure; and M&S [2]. ARL has the expertise and established capability in understanding the underlying penetration mechanics for a wide range of defeat mechanisms against improvised, shaped charge, kinetic energy (KE), explosively formed, and high-explosive munition threats. These mechanisms are intensively studied using HPC with physics-based M&S tools.

ARL's computational science facility, one of five DSRCs, features state-of-the-art, scalable, parallel architectures and large vector-parallel systems supporting both classified and unclassified missions throughout the DoD research, development, test, and evaluation community. Current DoD HPC systems at ARL have a cumulative capability of 1.1 petaFLOPS, and the facility is ranked in the top 15 of the world's most powerful computing sites [3].

The ARL DSRC, critical for protection research, has significant impact on armor R&D as it is used to study penetrator-target interactions that cannot be studied using experimental techniques. The center provides a significant enabling capability in high-fidelity numerical modeling and scientific visualization for armor/antiarmor simulations. An example simulation of a conical-shaped charge penetrating rolled homogeneous armor (RHA) steel is shown in Figure 5. This kind of shaped charge is typical of the warhead found within an RPG, and this kind of simulation is one of the first steps in the armor research and development process.

The jet collapse, jet formation, and penetration were predicted by CTH, a continuum mechanics code developed by Sandia National Laboratories. CTH software is just one of a variety of codes available at the ARL DSRC. HPC-driven M&S provides mechanistic understanding that can guide the development of new armor design options and lead to optimization of armor configurations. Novel computational techniques and material models are being developed and exploited to continually guide and inform armor development.

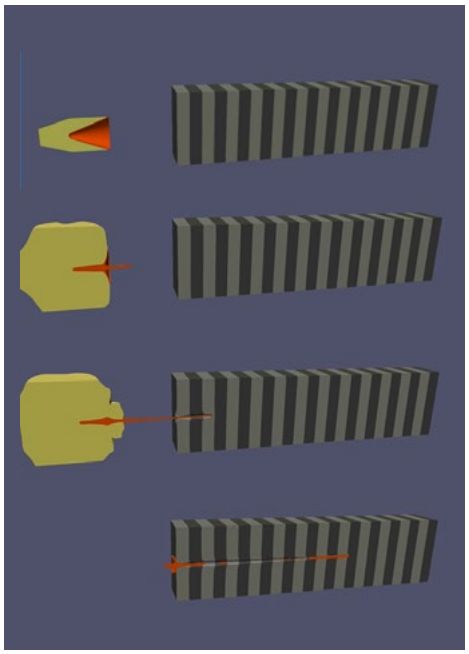

Figure 5: ARL DSRC Computational Prediction of a Shaped Charge Penetrating RHA Steel *(Photo Courtesy of ARL).*

ARL's computational science facility features state-of-the-art, scalable, parallel architectures and large vector-parallel systems supporting both classified and unclassified missions.

ARL's armor experimental facilities are used for development, validation, and verification of protection technology concepts, especially those developed via M&S. The experimental facilities are equipped for conducting detailed experiments using both chemical energy and KE munitions, including shaped charge warheads, EFPs, roadside IEDs, and blast penetrators, as well as small-, medium-, and large-caliber KE penetrators. The experimental facilities are highly instrumented to collect detailed information during the ballistics event. Example diagnostics include high-speed photography, digital image correlation, photon Doppler velocimetry, and high-fidelity flash radiography that can be used to measure flight parameters (position, velocity, yaw, and pitch), characterize penetrator morphology, and show some of the projectile-target interaction. Some examples of these capabilities are provided next.

Images from high-speed photography taken during an experiment of a blast penetrator warhead detonating and impacting a target at one of ARL's shaped charge armor experimental facilities are shown in Figure 6. This facility is used to evaluate passive, reactive, and electromagnetic armors being developed to defeat unitary and tandem shaped charge warheads and EFPs. Also used for shaped charge jet characterization and threat exploitations, it is capable of handling up to 20 lbs of high explosive.

Depending on the objective of the experiment, both static and dynamic warhead testing can be conducted at ARL's experimental facilities. A photograph of the dynamic RPG firing facility located at APG is shown in Figure 7. This facility is used to conduct experiments with dynamically-launched RPGs. The RPGs can either be launched free-flight or through ARL's own precision delivery system with precision target impact accuracy [3].

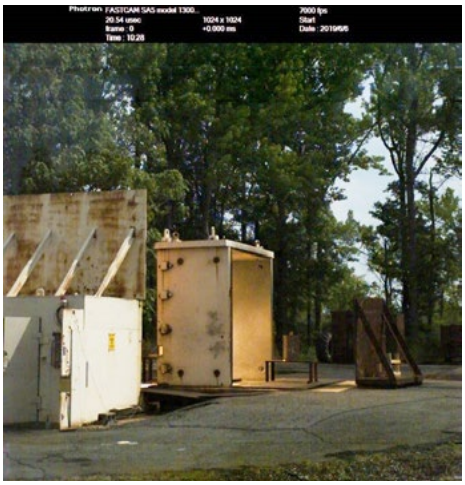

Figure 6: High-Speed Photography From an IED-EFP Event: Pre- (Left) and Post- (Right) Target Impact *(Photos Courtesy of ARL).*

Figure 7: Dynamic RPG Firing Facility *(Photo Courtesy of ARL).*

ARL has unique instrumentation capability for diagnosing armor experiments. Another example is the flash x-ray system shown in Figure 8. The multienergy, flash computed tomography system captures up to 15 flash x-ray images and, through tomographic reconstruction, produces three-dimensional (3-D) images of the armor/antiarmor interaction. Compared to a medical CT scan that takes several minutes or longer to gather enough information to produce a 3-D image, this flash x-ray system gathers the information in less than 1 millionth of a second, fast enough for the ballistics timescales required for this type of research. (A complete listing of ARL's facilities and capabilities can be found in reference 3.)

SUMMARY

ARL's combination of expert scientists and engineers, along with analytical, computational, and experimental resources, forms a unique collocated infrastructure to solve the Army's

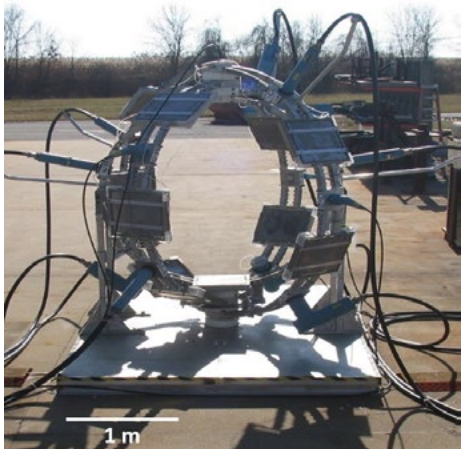

Figure 8: Three-Dimensional Flash X-ray System *(Photo Courtesy of ARL).*

protection technology needs. ARL researchers work closely with academia, industry, the intelligence and user communities, and program executive offices to develop and transition innovative protection technologies to the Warfighter. Advanced protection technology will continue to be needed as the last line of defense in order to dominate the close fight and enable the next-generation combat vehicle force to conduct multidomain operations. ■

REFERENCES

[1] Perconti, P. "ARL Overview." PowerPoint presentation, https://arlinside.arl.army.mil/inside/ default.cfm, accessed 25 March 2019.

[2] CCDC ARL. "Weapons & Materials Research." https://www.arl.army.mil/www/ default.cfm?page=35, accessed 25 March 2019.

[3] CCDC ARL. "Facilities of ARL." https://www.arl.army.mil/www/pages/172/docs/ ARLFacilitiesBook.pdf, accessed 25 March 2019.

[4] ARL DoD Supercomputing Resource Center. "About the ARL DSRC." https://www.arl.hpc.mil/about/, accessed 25 March 2019.

BIOGRAPHY

VALERIE WAGONER is a mechanical engineer within the Weapons and Materials Research Directorate at CCDC ARL, where her research interests include EFP and shaped charge jet defeat. She has been involved in the development of enhanced underbody protection for select U.S. ground vehicles, as well as IED-EFP add-on armor solutions and spall protection kits designed to protect U.S. troops against IEDs. She was recognized with the Army Research & Development Achievement Award for Excellence in a Technical Collaboration in 2010 and received the Achievement Metal for Civilian Service in 2017. She holds an M.S. and a B.S. in metallurgical and materials engineering from the University of Texas at El Paso.

DSIAC FEATURED EXPERT - *HARRY "RICK" LUZETSKY*

★★★★★

DSIAC would like to take a moment to recognize a subject matter expert who has provided users with valuable help and assistance.

HARRY "RICK" LUZETSKY is a subject matter expert at the SURVICE Engineering Company, with more than 30 years of experience in composites and more than 20 years of experience in survivability. With a specific expertise in design, test, and research and development, Mr. Luzetsky has helped develop and assess survivability features for numerous aircraft and has been active in composite design for vehicle performance and survivability improvements. He is the lead engineer for SURVICE's role in developing the thermoplastic drive shaft and is a coauthor of a pending patent on an advanced fuel containment technology and fiber reinforcement, structural composite, faraday cage enclosure for electronics. Mr. Luzetsky holds a B.S. in materials engineering from Drexel University.

Years of experience: 30+

Expertise: composites; survivability and vulnerability

Number of publications: 25+

Learn more about Rick Luzetsky: https://www.dsiac.org/resources/authors/harry-r-luzetsky ▸

Zero-Bias Broadband Ultraviolet Photoconductor Based on ULTRANANOCRYSTALLINE DIAMOND NANOWIRE ARRAYS

By Rafael Velázquez, Manuel Rivera, Andrew F. Zhou, David Bromley, and Peter X. Feng

Diamond Nanowires (Photo Source: William Gilpin)

SUMMARY

This article focuses on developing a broadband ultraviolet (UV) photodetector (PD) based on superflat, boron-doped ultrananocrystalline diamond (UNCD) nanowire (NW) arrays functionalized with platinum (Pt) nanoparticles and capable of withstanding high operating temperatures. This PD exhibits an extremely large responsivity (1,224 A/W) to 300-nm light radiation at zero bias while taking advantage of diamond's unique stability from its ability to function at temperatures as high as 200 °C. Additionally, it has a fast response time of 17 ms.

INTRODUCTION

Current needs in applications, such as space exploration and Earth's surface incident radiation monitoring, have imposed new requirements on the next generation of deep UV detectors. In particular, reduced energy consumption, enhanced resistance to the performance degradation at high temperatures, and high portability appear to be extremely important properties for a growing demand of crucial applications [1]. Recent progress has been made toward achieving these goals. Several nanostructured, wide band-gap, materials-based detectors have been developed [2–4]. However, designing a multifunctional material that simultaneously exhibits desired properties in PDs still remains a challenge.

We aim at creating a cost-effective, high-performance UNCD-based UV PD that satisfies the market needs of high-temperature and self-power operation. Diamond has attracted significant interest as a promising candidate for UV sensing applications due to its wide band gap, chemical stability, and robustness. Diamond also has excellent mechanical hardness and tunable band gap via doping [5, 6]. The undoped, single-crystal diamond has a band gap of 5.5 eV [7, 8]. Lansley and his group used natural and synthetic diamond to achieve a very fast time response (less than a microsecond) when these detectors were radiated with pulsed laser beams [9]. Pace and De Sio used both single crystalline and polycrystalline diamond films to develop two types of photoconductive detectors [10]. The obtained experimental data suggested that single crystalline, diamond-based detectors had much higher sensitivity than the PD using polycrystalline diamond [11, 12].

Diamond has attracted significant interest as a promising candidate for UV sensing applications due to its wide band gap, chemical stability, and robustness.

However, natural single crystalline diamond is very expensive, whereas either nanocrystalline diamond or micropolycrystalline diamond films have rough surfaces with which no precise nanostructures for electronic devices can be made. In contrast, UNCD has excellent film thickness uniformity with extremely low surface roughness independently of its film thickness. Furthermore, UNCD can be obtained from a reliable and cost-effective production method yielding consistent UNCD material properties.

Our research focuses on the functionalization of superflat UNCD material with Pt nanoparticles from which NW arrays have been fabricated for developing novel, self-powered UV PD devices. We base this research on the fact that Pt nanoparticle-functionalized, UNCD NW-based PDs would drastically improve the response times because of their large surface-to-volume ratios. One-dimensional UNCD NW nanostructures with Pt particles on the surface of the NWs are essential blocks to fabricate a field-effect transistor (FET).

The Pt on the surface of the NWs may change the conductance by changing the surface charges and states. This changes the gate potential, work function, and band alignment, resulting in a gate coupling and change in carrier mobility. All of these will be regarded as a floating gate effect on the conducting channel of the FET.

The strong local electric field at the reversely-biased Schottky barrier area will quickly separate the photon-generated electrons and holes, reducing the electron-hole recombination rates. This reduces the power consumption, increases the portability, and enhances the signal-to-noise ratio [13]. The obtained experimental data clearly indicate that the newly-designed PD exhibits high photocurrent and outstanding responsivity to both UVB and UVC radiations at zero-applied voltage while taking advantage of diamond's unique stability to function at temperatures as high as 300 °C. Additionally, the investigated PD has fast response times less than 17 ms. Few materials reported so far, if any, possess such a desirable set of UV-sensing performance characteristics.

SYNTHESIS

The boron-doped UNCD thin films were synthesized by Advanced Diamond Technologies, Inc., with the microwave plasma, chemical vapor deposition system (Lambda Technologies Inc.) using a standard deposition procedure. They

were grown at a substrate temperature of 760 °C, a microwave power of 2100 W, and an $Ar/CH_4/H_2$ gas mixture, with flow rates of 400/1.2/8 sccm, respectively. Throughout the UNCD deposition, the chamber pressure was maintained at 120 mbar. The growth procedure was performed on a silicon wafer substrate for 1 hr, resulting in an 80-nm-thick UNCD film deposition. As a source of boron, trimethylboron was used (i.e., B[CH3]3) for the doping. (For more details regarding the synthesis process of UNCD growth and the doped process, see references 14–17.)

UNCD NW arrays (70 nm wide and 35 µm long) were then fabricated using top-down-based lithography techniques. (A detailed description of the crystalline structure and surface morphology characterization, electron beam lithography, and NW array fabrication can be found in references 11, 12, and 18.)

Finally, using a sputtering method, 10-nm aluminum (Al)/100-nm Pt pairs were deposited as electrodes (ohmic contacts) onto two sides of the UNCD NW arrays. In the process, Pt nanoparticles functionalized on the surface of UNCD NWs, resulting in individual punctual Schottky contacts in the NW's surface. The fabricated NW device was then annealed with a LakeShore temperature controller at 150 °C for 5 min in the probe station chamber.

At zero bias, no induced photocurrent could be detected from the two ohmic, contact-based PDs exposed to deep UV light radiation. The carrier transport of UNCD that relied on hopping transport mechanisms resulted in a low carrier velocity. In other words, the UNCD films-based PDs had very poor performance. Therefore, very few groups have worked on them, even though UNCD is much cheaper than single-crystal diamond.

At zero bias, no induced photocurrent could be detected from the two ohmic, contact-based PDs exposed to deep UV light radiation.

We used Pt nanoparticles to functionalize the surface of UNCD NWs in an attempt to improve the performance of a UNCD-based PD. The prototype formed a nonsymmetrical Schottky contact device containing a Schottky barrier (SB) contact at one side of the device and an ohmic contact at the other side for each Pt nanoparticle on the UNCD wire surface. The entire device could be regarded as an NW connected in series with an SB diode (one for each Pt nanoparticle).

The Schottky contact area in each wire constituted the bottleneck for the current transport in the device. The original SB height φ_{SB} was determined by the work-function difference between the metal and Pt nanoparticles on the surface of the UNCD wires and the interface states. The current passing through the Schottky contact was very sensitive to the Schottky barrier height and width. Light irradiation at or near the SB area could change the local electric-field distribution and thus cause the variations of the SB height and width, resulting in a detectable current change [13, 19].

SEM Images

Figure 1a shows the SEM image of the fabricated UNCD NWs, which are nearly 35 µm long and connected to the Al/Pt electrodes. The gap is approximately 1 µm between the UNCD NWs. Figure 1b shows an enlarged SEM image of a typical single wire consisting of tiny UNCD nanoparticles, with a diameter of about 50 to 70 nm. The UNCD NWs have an average width of 70 nm. (A detailed characterization of the UNCD with a high-resolution transmission, electron microscope can be found in previous reports [11, 12].)

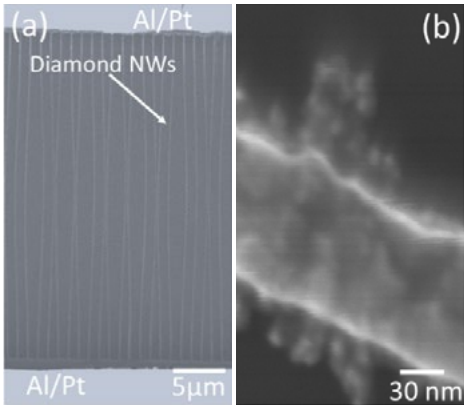

Figure 1: (a) SEM Image of the UNCD NW Array and (b) Enlarged Image of a Single UNCD NW *(Source: R. Velázquez).*

Raman Spectroscopy

Raman scattering is a powerful, semiquantitative method to examine the diamond structure because the sp^2 and sp^3 carbon bondings are very sensitive to this scattering. Figure 2 shows a typical Raman spectrum of the boron-doped UNCD wire arrays by using a triple monochromator with an excitation wavelength of 514 nm from an Ar^+ ion laser and a microscope to focus the laser beam onto the NWs. Two broad bands assigned to the regular D and G bands are clearly visible at 1332 cm^{-1} and 1595 cm^{-1}, respectively.

Normally, the G band is from the sp^2 carbon bonds, indicating the synthesized sample is a carbon-mixed UNCD material. The broad Raman spectral intensity taken at the D band (1332 cm^{-1}) from sp^3 carbon bonds

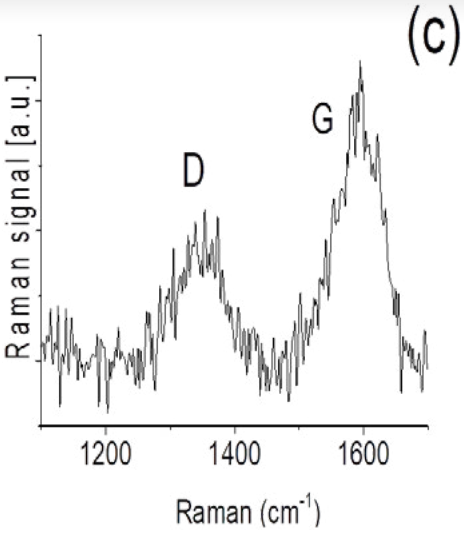

Figure 2: Typical Raman Spectrum of the Boron-Doped UNCD Wire Array *(Source: R. Velázquez).*

proves that the material is indeed diamond. A broadened profile of the D band could be related to the polycrystalline structure of randomly-oriented grains or the nanoscale effect [20].

PROTOTYPE

To understand the electrical properties, the fabricated UNCD NWs were connected to a basic electric circuit to form the prototype. Figure 3 shows a schematic diagram of the prototypical PD. Two external conductive electrodes installed at two ends of UNCD NWs were

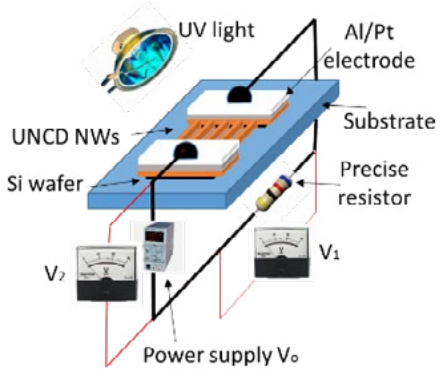

Figure 3: Schematic Setup of the Prototype *(Source: R. Velázquez).*

serially connected to a precision resistor $R_{precise}$, a switcher, and a step-up/step-down voltage regulator V_o (Keysight E3643A power supply). The setup also consisted of two Hewlett-Packard 34401A programmable electronic multimeters (V_1 and V_2) monitored by a LabVIEW program from which the variations of the two voltages ($V_{prototye} = V_2 - V_1$) and the current ($I_{prototype} = V_1/R_{precise}$) in the prototype were recorded. A tungsten filament and a thermocouple were used as a controllable heater for obtaining a desired operating temperature.

ELECTRICAL PROPERTIES

Even though we focus on the ability of the PD to operate at zero bias (for this case, $V_2 = 0$), it is still necessary to understand how the bias affects the properties of the UNCD NWs-based detector. Figure 4 shows typical responses at different reverse biases when the UNCD NWs-based PD is cycled, with 2 min between the "switch-on" and "switch-off" of the 250-nm UV light radiation at room temperature. In Figure 4a, the fabricated PD displays a quick, well-defined response. A higher-bias voltage yields a higher-induced photocurrent and a larger responsivity ratio between the output photocurrent and the input UV light power.

As seen in Figure 4b, the obtained photocurrents (I_{ph}) at –1, –2, and –2.5 V bias with and without UV radiation are approximately 6, 14, and 29x larger, respectively, than at zero bias. This characteristic was much better than the SiC, diamond, and other oxide semiconductors-based detectors, although the measurements were taken at a higher bias [21–24]. Furthermore, fast response and recovery times were observed, regardless of the applied bias.

A slight variation of the baseline was also observed in Figure 4a, as the

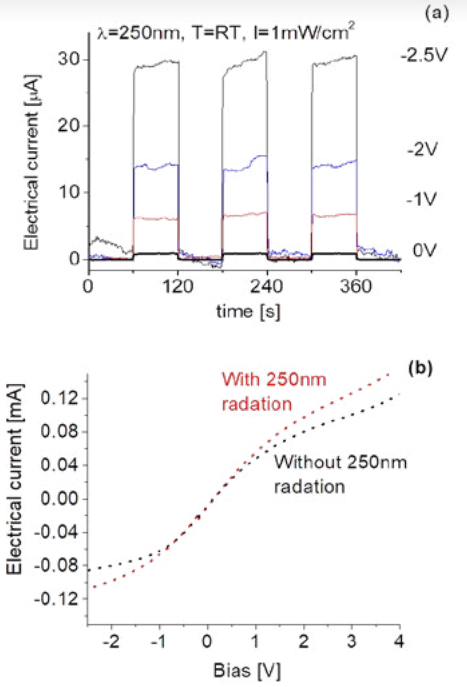

Figure 4: (a) Bias Effect on the Response and (b) the Electrical Current as a Function of Bias *(Source: R. Velázquez).*

reverse bias from the power supply increased. Following an increase of bias magnitude, the dark current unavoidably increased, as well as the noise level. Therefore, the signal-to-noise ratio did not improve significantly as the bias magnitude increased. Figure 4b shows the typical current-voltage reverse bias characteristics in dark and 250-nm UV light at room temperature. A nonlinear current-voltage curve was observed at the applied bias, indicating a Schottky diode behavior of the NWs/Pt contacts.

Characterization Responsivity

When the PD is exposed to UV light, the photonic energy is absorbed by the valence electrons, leading to the induced photocurrent. Three different UV wavelengths were used for characterizing the responsivity of the boron-doped UNCD NWs. The intensity of the UV light onto the surface of the PD was controlled by shifting the height between the UV light source and the detector. Figure 5 illustrates typical

photoresponses of the fabricated UV PD to 250-, 300-, and 350-nm UV light illuminations, respectively, subjected to the on/off cycles with 120 s. Results of the UV PD presented in Figure 5 were tested at room temperature under three different incident radiation intensities.

Figure 5a shows the photoresponses at zero bias and room temperature when the prototype was exposed to 250-nm light illumination cycling with 120 s. When the detector was exposed to UV light radiation, the induced photocurrent quickly increased and reached a stable maximum value. When the UV radiation switched off, the photocurrent decreased to zero value. Excellent features in repeatability and stability are clearly visible. The induced photocurrent can be attributed to the absorption of UV photons by the active UNCD NW's material.

A decrease in photocurrent magnitude was expected as the intensity of UV light reaching the surface of the PD decreased. However, no significant change in photocurrent was observed when the UV intensity ranged from 1 mW/cm^2 to 0.03 mW/cm^2, indicating that the detector might be saturated with UV radiation. Under this condition, the generated photocurrent from the UV PD reached 0.94 µA. Since the average length and width of each NW was 35 µm and 70 nm and the total number of NWs in the platform was 100, we estimated a total exposure area of 245 µm^2 for the present prototype. Consequently, we obtained a responsivity around 406 A/W for 300-nm UV light. This value was at least three orders of magnitude higher than what has been reported so far on zero-bias or self-powered, deep UV PDs made of different materials [3, 4, 15].

When the detector was exposed to UV light radiation, the induced photocurrent quickly increased and reached a stable maximum value.

Similar phenomena, including good repeatability and stable baseline, were also observed when the PD was exposed to 300 nm of UV light illumination (shown in Figure 5b). The main observed difference was that the 300-nm induced photocurrent was almost 3x larger than that induced with 250-nm light illumination. As a result, an extremely high responsivity up to 1,224 A/W was obtained from the present PD when exposed to 300-nm light.

The total size of the platform used was only 0.5 mm^2, which was much smaller than those UV detectors reported by others. From the literature, several groups were successful in achieving very high responsivity from nanomaterials-based PDs in the UV region at a high applied bias. This has the disadvantage of increasing dark current level, resulting in a poor signal-to-noise ratio. Furthermore, neither size nor weight of a bias-based detector could be reduced easily due to the power supply constraint. In contrast, the self-power, zero-bias PDs tended to exhibit low, dark current magnitudes [25–29]. In the present case, the obtained dark current was only 2 × 10^{-7} A. Since the induced current was 3.5 µA, we had a signal-to-noise ratio of 18. Because it did not require an external power supply, the detector could be much smaller. The miniaturization of PD devices was extremely important for a wide number of space applications.

Characterizations of the time-dependent photoresponsivity of the fabricated detector at zero bias and room temperature when exposed to 350-nm light illumination were also achieved. The results are shown in Figure 5c.

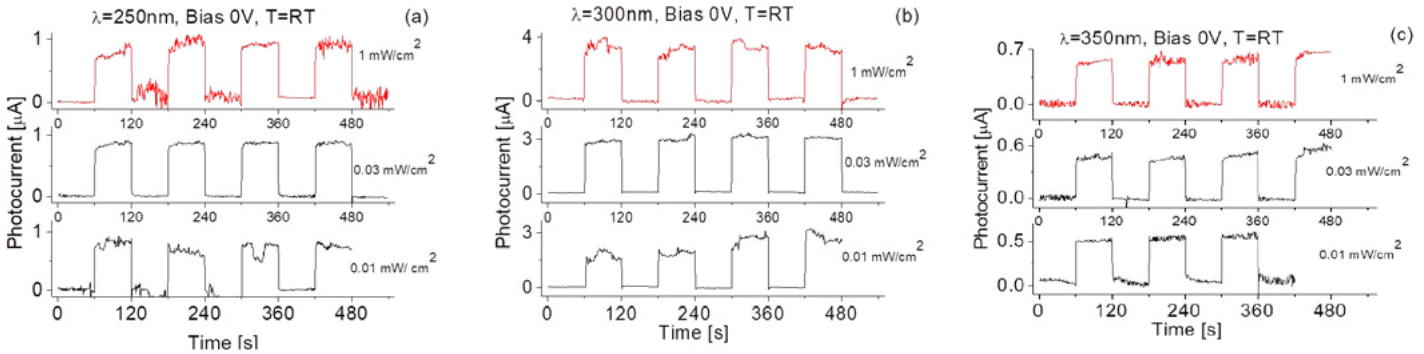

Figure 5: Time-Dependent Photoresponsivity at Zero Bias and Room Temperature Under (a) 250-, (b) 300-, and (c) 350-nm Light Radiations at Different Intensities *(Source: R. Velázquez).*

Excellent repeatability and stability, as well as quick response time, are still clearly visible. However, the obtained 350-nm light-induced photocurrent was almost 6x less than that induced by 300-nm light. Correspondingly, a responsivity of 244 A/W related to 350-nm radiation was obtained.

As shown in Figure 5, the responsivity of the present boron-doped, UNCD-based PD is highly related to the wavelength of UV light radiation. The highest responsivity of 1,224 A/W is related to the 300-nm UV light illumination. Applying Mendoza's model to the obtained relationship between the responsivity strength and wavelength of UV light radiation, we estimated that the present boron-doped UNCD had a band-gap energy around 4.1 eV (~300 nm) [30]. This agreed with the previous studies of the band-gap shift obtained from the basic characterization of UNCD [31, 32].

Temperature Effect

The photoresponse of the UNCD-based UV sensor was also studied at different operating temperatures. The results, presented in Figure 6, were conducted with a 250-nm wavelength UV light radiation. The vast majority of UV PDs reported were inoperable at temperatures above 100 to 150 °C [23]. The UNCD-based PD continued to perform well above this temperature limit. Comparing the responses obtained at room temperature in Figure 5 with higher temperatures in Figure 6 revealed that the photocurrent decreased with increasing temperature. In addition to a decrease in signal-to-noise ratio, this was expected due to the unavoidable increase in dark current and thermal noise as the temperature increased.

However, as shown in Figure 6, the UNCD prototype maintains an excellent repeatability and stability as operating temperature is increased up to 100 °C. The PD under investigation was capable of withstanding operating temperatures as high as 200 °C while retaining a clear, stable, and reproducible signal well above the thermal noise threshold. Further increasing the temperature to 300 °C, the light-induced photocurrent response from the PD is still measurable, even with the large thermal noise contribution. This is a considerable increase in PD heat tolerance, compared to the majority of UV sensors reported, and is directly attributed to diamond's intrinsic properties.

Similar results for the PD prototype under investigation were obtained upon exposition to 300- and 350-nm radiations. As seen in Figure 7, at an operating temperature of 100 °C, the UNCD-based PD experiences a slight decrease in photocurrent compared to its room-temperature performance. However, the signal-to-noise ratio is still significantly high, and the fast response times were not affected. Also, at an operating temperature of 100 °C, the PD prototype still exhibited high responsivity values when exposed to 250-, 300-, and 350-nm radiations.

Response Time and Recovery Time

The UNCD-based PD exhibited fast response and recovery times regardless of the incident radiation at operating temperatures up to 200 °C. To further investigate the characteristic response and recovery times (tres and trec) of the prototype, high time-resolution measurements were performed. Determining the tres values was based on the time interval for the photocurrent to rise to 90% of its peak value and trec as the time interval for the signal to decay to 10% of its peak value.

Figure 8 shows typical measurements of both t_{res} and t_{rec} when the 250-nm light illumination is turned on and off at room temperature. The PD under investigation exhibits a response time of 17 ms. On the other hand, t_{rec} is around 30 ms, almost twice the response time

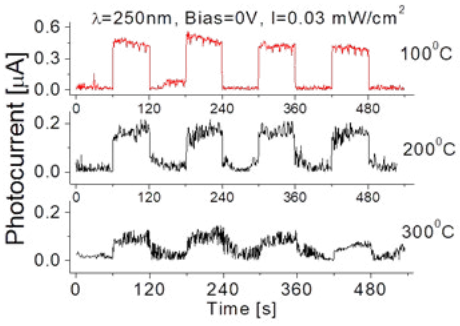

Figure 6: Temperature Effect on the UV PD's Photo Response When Exposed to 250-nm Light *(Source: R. Velázquez).*

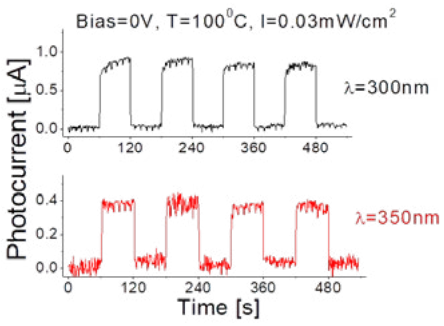

Figure 7: Temperature Effect on the UV PD's Responsivity to 300- and 350-nm Light When Operated at 100 °C *(Source: R. Velázquez).*

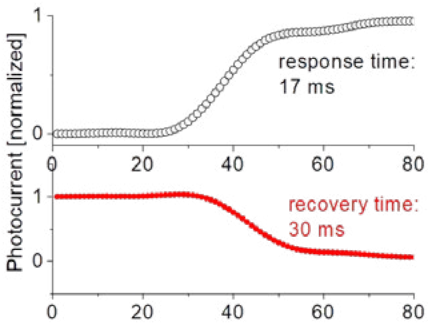

Figure 8: Response and Recovery Times of the Boron-Doped, UNCD-Based UV PD *(Source: R. Velázquez).*

t_{res}. This is likely due to the intrinsic radiation intensity decay of the light source as it switches off. Even though the obtained rise and decay times of the UNCD-based PD cannot compare to those of the reported single-crystalline, diamond-based PD, the present UNCD NW-based PD still shows it advantages, including a cost-effective, self-powered feature and higher responsivity. Nevertheless, the obtained response times are still much faster than most reported PDs with similar responsivity values [33, 34].

CONCLUSIONS

Based on the superflat surface, synthesized UNCD boron-doped film, a precise UNCD NW array was designed and fabricated. To the best of our knowledge, this was the first demonstration of the zero-bias, solar-blind PDs based on Pt nanoparticle-functionalized, boron-doped UNCD NW arrays providing ultra-high responsivities up to 406, 1,224, and 244 A/W at 250-, 300-, and 350-nm UV wavelengths, respectively.

The newly-developed PD possesses outstanding features in quick response (less than 17 ms), with excellent repeatability and stability. Experimental data also showed that an extremely large responsivity could be achieved with a high reverse bias. The obtained photocurrents were almost 6, 14, and 29x larger at –1, –2, and –2.5 V bias, respectively, than at zero bias. These characteristics were much better than those reported for SiC, diamond, and other oxide semiconductors-based, zero-bias, solar-blind PDs. In addition, the PD based on UNCD NW arrays performed extremely well, even at temperatures as high as 200 °C, making the UNCD NW array arrangement an ideal candidate for UV sensing applications in harsh environments. ■

Experimental data also showed that an extremely large responsivity could be achieved with a high reverse bias.

ACKNOWLEDGMENTS

This work was financially supported by the National Science Foundation's Centers of Research Excellence in Science and Technology for Innovation, Research, and Education in Environmental Nanotechnology, grant no. HRD-1736093. The authors also want to acknowledge the help of Ali Aldalbahi, Xinpeng Wang, and the Naval Air Warfare Center Aircraft Division (NAWCAD) 4.5.14 for their support.

REFERENCES

[1] Wang, Z. L. "Self-Powered Nanosensors and Nanosystems." *Adv. Mat.*, vol. 24, no. 2, pp. 280–285, 2012.

[2] Hao, L. Z., Y. J. Liu, W. Gao, Z. D. Han, Z. J. Xu, Y. M. Liu, and J. Zhu. "Self-Powered Photosensing Characteristics of Amorphous Carbon/Silicon Heterostructures." *RSC Adv.*, vol. 6, no. 46, pp. 40192–40198, 2016.

[3] Chen, H., P. Yu, Z. Zhang, F. Teng, L. Zheng, K. Hu, and X. Fang. "Ultrasensitive Self-Powered Solar-Blind Deep-Ultraviolet Photodetector Based on All-Solid-State Polyaniline/MgZnO Bilayer." *Small*, vol. 12, no. 42, pp. 5809–5816, 2016.

[4] Tsai, D., W. Lien, D. Lien, K. Chen, M. Tsai, D. G. Senesky, Y. Yu, A. P. Pisaro, and J. He. "Solar-Blind Photodetectors for Harsh Electronics." *Sci. Rep.*, vol. 3, p. 2628, 2013.

[5] Ashfold, M. N. R., P. W. May, C. A. Rego, and N. M. Everitt. "Thin Film Diamond by Chemical Vapour Deposition Methods." *Chemical Society Review*, vol. 23, pp. 21–30, 1994.

[6] Chen, Q., D. M. Gruen, A. R. Krauss, T. D. Corrigan, M. Witek, and G. M. Swain. "The Structure and Electrochemical Behavior of Nitrogen-Containing Nanocrystalline Diamond Films Deposited From CH4/N2/Ar Mixtures." *Journal of The Electrochemical Society*, vol. 148, pp. E44–51, 2001.

[7] Liua, Z., J.-P. Ao, F. Lia, W. Wanga, J. Wangd, J. Zhanga, and H.-X. Wanga. "Photoelectrical Characteristics of Ultra Thin TiO_2/Diamond Photodetector." *Materials Letters*, vol. 188, pp. 52–54, 2017.

[8] Balducci, A., M. Marinelli, E. Milani, M. E. Morgada, A. Tucciarone, G. Verona-Rinati, M. Angelone, and M. Pillon. "Extreme Ultraviolet Single-Crystal Diamond Detectors by Chemical Vapor Deposition." *Appl. Phys. Lett.*, vol. 86, p. 193509, 2005.

[9] Lansley, S. P., G. T. Betzel, P. Metcalfe, L. Reinisch, and J. Meyer. "Comparison of Natural and Synthetic Diamond X-ray Detectors." *Australas Phys. Eng. Sci. Med.*, vol. 33, no. 4, pp. 301–306, 2010.

[10] Pace, E., and A. De Sio. "Innovative Diamond Photo-Detectors for UV Astrophysics." *Mem. S.A.It. Suppl.*, vol. 14, pp. 84–89, 2010.

[11] Roberson, J., et al. "Diamond-Like Amorphous Carbon." *Mater. Sci. Eng. R-Pep.*, vol. 37, nos. 4–6, pp. 129–281, 2002.

[12] Piazza, F., J. A. Gonzalez, R. Velazquez, J. De Jesus, S. A. Rosario, and G. Morell. "Diamond Film Synthesis at Low Temperature." *Diamond Relat. Mater.*, vol. 15, no. 1, pp. 109–116, 2006.

[13] Hu, Y., J. Zhou, P. H. Yeh, Z. Li, T. Y. Wei, and Z. L. Wang. "Supersensitive, Fast-Response Nanowire Sensors by Using Schottky Contacts." *Adv. Mater.*, vol. 22, pp. 3327–3332, 2010.

[14] Zeng, H., P. Arumugam, S. Siddiqui, and J. Carlisle. "Low Temperature Boron Doped Diamond." *Applied Physics Letters*, vol. 102, p. 223108, 2013.

[15] Wang, X. "Synthesis, Fabrication, Characterization, and Application of Ultranano Crystalline Diamond Micro and Nanostructures." Ph.D. Thesis, Physics Department, University of Puerto Rico, San Juan, PR, 2012.

[16] Wang, X., L. E. Ocola, R. S. Divan, and A. V. Sumant. "Nanopatterning of Ultrananocrystalline Diamond Nanowires." *Nanotechnology*, vol. 23, no. 7, pp. 1–7, 2012.

[17] Zeng, H., A. Konicek, N. Moldovan, F. Mangolini, T. Jacobs, I. Wylie, P. Arumugam, S. Siddiqui, R. Carpick, and J. Carlisle. "Boron-Doped Ultrananocrystalline Diamond Synthesized With an H-Rich/Ar-Lean Gas System." *Carbon*, vol. 84, pp. 103–117, 2015.

[18] Auciello, O., and A. V. Sumant. "Status Review of the Science and Technology of Ultrananocrystalline Diamond (UNCD) Films and Application to Multifunctional Devices." *Diamond Relat. Mater.*, vol. 19, nos. 7–9, pp. 699–718, 2010.

[19] Lee, C. H., S. Qin, M. A. Savaikar, J. Wang, B. Hao, D. Zhang, D. Banyai, J. A. Jaszczak, K. W. Clark, J.-C. Idrobo, A.-P. Li, and Y. K. Yap. "Room-Temperature Tunneling Behavior of Boron Nitride Nanotubes Functionalized With Gold Quantum Dots." *Adv. Mater.*, vol. 25, p. 4544, 2013.

[20] Tsujimoto, Y., Y. Matsushita, S. Yu, K. Yamaura, and T. Uchikoshi. "Size Dependence of Structural, Magnetic, and Electrical Properties in Corundum-Type Ti2O3 Nanoparticles Showing Insulator-Metal Transition." *Journal of Asian Ceramic Societies*, vol. 3, no. 3, pp. 325–333, 2015.

[21] Velázquez, R., A. Aldalbahi, M. Rivera, and P. Feng. "Fabrications and Application of Single Crystalline GaN for High-Performance Deep UV Photodetectors." *AIP Adv.*, vol. 6, no. 085117-1-12, 2016.

[22] Rivera, M., R. Velázquez, A. Aldalbahi, A. F. Zhou, and P. Feng. "Self-Powered 2D Boron Nitride Nanosheets Based Broadband UV Photodetectors for Hazardous Environments." *Sci. Rep.*, vol. 7, no. 42973, 2017.

[23] Aldalbahi, A., E. Li, M. Rivera, R. Velazquez, T. Altalhi, X. Peng, and P. A. Feng. "New Approach for Fabrications of SiC Based Photodetectors." *Sci. Rep.*, vol. 6, no. 23457, 2016.

[24] Peng, L., L. Hu, and X. Fang. "Low-Dimension Nanostructure Ultraviolet Photodetector." *Adv. Mater.*, vol. 25, pp. 5321–5328, 2013.

[25] Hu, P., L. Wang, M. Yoon, J. Zhang, W. Feng, X. Wang, Z. Wen, J. C. Idrobo, Y. Miyamoto, and D. B. Geohegan. "Highly Responsive Ultrathin GaS Nanosheet Photodetectors on Rigid and Flexible Substrates." *Nano Letters*, vol. 13, no. 4, pp. 1649–1654, 2013.

[26] Yang, S., Y. Li, X. Wang, N. Huo, J.-B. Xia, S.-S. Li, and J. Li. "High Performance Few-Layer Gas Photodetector and Its Unique Photo-Response in Different Gas Environments." *Nanoscale*, vol. 6, no. 5, pp. 2582–2587, 2014.

[27] Hu, L., J. Yan, M. Liao, H. Xiang, X. Gong, L. Zhang, and X. Fang. "An Optimized Ultraviolet-A Light Photodetector With Wide-Range Photoresponse Based on ZnS/ZnO Biaxial Nanobelt." *Advanced Materials*, vol. 24, no. 17, pp. 2305–2309, 2012.

[28] Wu, J., G. K. W. Koon, D. Xiang, C. Han, C. T. Toh, E. S. Kulkarni, I. Verzhbitskiy, A. Carvalho, A. S. Rodin, and S. P. Koenig. "Colossal Ultraviolet Photoresponsivity of Few-Layer Black Phosphorus." *ACS Nano.*, vol. 9, no. 8, pp. 8070–8077, 2015.

[29] Li, L., P. S. Lee, C. Yan, T. Zhai, X. Fang, M. Liao, Y. Koide, Y. Bando, and D. Golberg. "Ultrahigh-Performance Solar-Blind Photodetectors Based on Individual Single-Crystalline $In_2Ge_2O_7$ Nanobelts." *Adv. Mat.*, vol. 22, no. 45, pp. 5145–5149, 2010.

[30] Mendoza, F., V. Makarov, B. Weiner, and G. Morell. "Solar-Blind Field-Emission Diamond Ultraviolet Detector." *Appl. Phy. Lett.*, vol. 107, no. 201605-1-5, 2015.

[31] Sankaran, K. J., K. Panda, B. Sundaravel, H.-C. Chen, I.-N. Lin, C.-Y. Lee, and N.-H. Tai. "Engineering the Interface Characteristics of Ultrananocrystalline Diamond Films Grown on Au-Coated Si Substrates." *ACS Appl. Mater. Interfaces*, vol. 4, no. 8, pp. 4169–417, 2012.

[32] Franta, D., L. Zajíčková, M. Karásková, O. Jašek, D. Nečas, P. Klapetek, and M. Valtr. "Optical Characterization of Ultrananocrystalline Diamond Films." *Diamond & Related Materials*, vol. 17, pp. 1278–1282, 2008.

[33] Dhanabalan, S. C., J. S. Ponraj, H. Zhang, and Q. Bao. "Present Perspectives of Broadband Photo-Detectors Based on Nanobelts, Nanoribbons, Nanosheets and the Emerging 2D Materials." *Nanoscale*, vol. 8, no. 12, pp. 6410–6434, 2016.

[34] Feng, P., X. Wang, A. Aldalbahi, and A. F. Zhou. "Methane Induced Electrical Property Change of Nitrogen Doped Ultrananocrystalline Diamond Nanowires." *Appl. Phys. Lett.*, vol. 107, no. 23, p. 233103, 2015.

BIOGRAPHIES

RAFAEL VELÁZQUEZ works at NAWCAD, Airborne Anti-Submarine Warfare Systems Engineering Division, Patuxent River, MD. He has performed fundamental research in nanomaterials for light harvesting, photovoltaics, energy storage, microcrystalline diamond, ultrananocrystalline diamond nanowire arrays in deep UV photodetection, and nanomaterials for biomedical applications in bacteria and cancer cells. He was also associate professor at the Molecular Sciences Research Center for the Biomedical Applications of Nanomaterials Research Lab. He has written more than a dozen publications. Dr. Velázquez holds a Ph.D. in chemical physics from the University of Puerto Rico.

MANUEL RIVERA is the leading investigator in a National Institutes of Health Small Business Innovation Research grant with Sil Technologies in collaboration with the University of Puerto Rico Mayaguez Campus. He has performed fundamental research in molecular dynamics of liquid crystals and polymers subjected to nanoconfinement and contributed to the advancement in novel applications of tailored nanomaterials. He has investigated the use of polymer-carbon nanotube metacomposites in gas detection and boron nitride nanosheets in deep UV photodetection and written more than a dozen publications. Dr. Rivera received his Ph.D. in chemical physics.

ANDREW F. ZHOU is a professor at the Indiana University of Pennsylvania, Indiana, PA. His research interests include solid-state lasers and nanophotonics. He has held postdoctoral positions at the University of Strathclyde, Glasgow University, and Imperial College in the United Kingdom. He has worked as a research scientist in the United States and assistant professor at Nanyang Technological University in Singapore. Dr. Zhou holds a Ph.D. in optics.

DAVID BROMLEY works at NAWCAD, Airborne Anti-Submarine Warfare Systems Engineering Division, Patuxent River, MD. He has 25 years of experience in underwater acoustics, magnetics, and sonobuoys and is a Naval Air Systems Command Associate Fellow. Dr. Bromley holds a Ph.D. in physics from Drexel University, with a physics specialty in laser dynamics.

PETER X. FENG is a professor in the Department of Physics, University of Puerto Rico. His research interests include semiconducting and ceramic materials and various types of electronic devices, including field emission displays; gas, humidity, and thermal sensors; Schottky diodes; photodetectors; sensor calibration systems; and digitally-controlled pulse deposition systems. He has authored more than 190 articles. Dr. Feng holds a Ph.D. in physics from LaTrobe University.

(Photo Source: 123rf.com)

Change Detection in Satellite Imagery With

REGION PROPOSAL NETWORKS

By Andreas Savakis, Navya Nagananda, John P. Kerekes, Emmett J. Ientilucci, Russell Blue, William Hicks, Todd V. Rovito, and Erik Blasch

SUMMARY

This article presents a deep learning approach called Proposal-based Efficient Adaptive Region Learning (PEARL) to change detection (CD) in satellite imagery based on region proposal networks. Region proposals are useful for selecting regions of interest in convolutional networks used for object detection and localization. The generated region proposals compare object-like characteristics in target and reference images taken at different times. The effectiveness of the PEARL approach is demonstrated with an airplane dataset generated by physics-based synthetic data from Digital Imaging and Remote Sensing Image Generation (DIRSIG).

INTRODUCTION

Change Detection

The dramatic proliferation of satellite images that require inspection has increased the demand for automating challenging tasks, including CD, to assist analysts. Detecting changes in satellite images of the same location, but observed at different times, is important in surveillance and security, disaster management, demographic estimation, crop monitoring, and other important applications.

However, CD remains a challenging problem because of the wide variation of potential changes of interest, including environment illumination, atmospheric changes, weather conditions, seasonal variations, and other factors such as sensor resolution and noise. Hence, there is a need for algorithm robustness against changing operating conditions. To deal with this complexity, data-driven approaches collect as many representative examples as possible, while model-driven approaches generate synthetic data based on the fundamental physics of the sensor, environment, and target (SET) operating conditions.

The task of CD can be broadly categorized into three types—structured, unstructured, and semistructured. *Structured* CD works by identifying changes in known object classes (e.g., the movement of vehicles or aircraft on the ground). These known classes are used to label data and are explicitly included in the training dataset seeding the algorithms. The Siamese network shown in Figure 1 is an example of a model [1] trained to detect vehicles, helicopters, or other objects of interest. *Unstructured* CD is more general and difficult, as the desired objects are unlabeled and include wider variations, such as piles of materials (dirt or coal), construction sites, or containers at a port. The difficulty with unstructured CD is due to changes of interest not anticipated in advance or incorporated in the training data. *Semistructured* CD approaches have a small set of labeled data from a subject matter expert that seed the algorithm to learn subtle variations without requiring a large amount of labeled data for training.

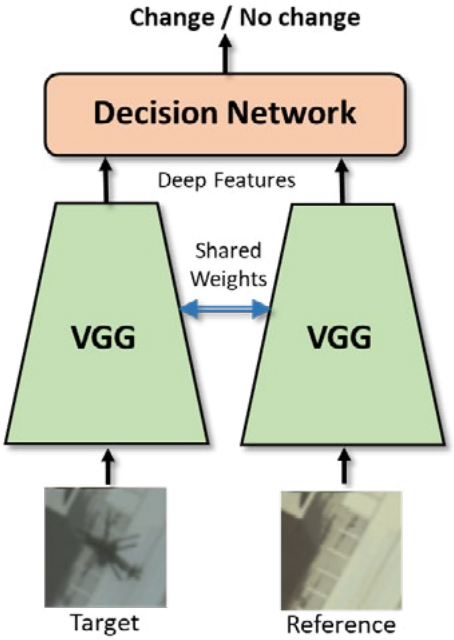

Figure 1: Siamese CD Network Trained With DIRSIG-Generated Image Chips of Helicopters and Backgrounds *(Source: Rochester Institute of Technology [RIT]).*

The dramatic proliferation of satellite images that require inspection has increased the demand for automating challenging tasks to assist analysts.

DIRSIG Data Generation

Another challenge with CD is that datasets for algorithm training and testing are not readily available, and collecting and annotating them is a laborious task. We address this need by utilizing DIRSIG [2] to generate datasets for training or testing our models. DIRSIG is a physics-driven synthetic image generation model developed by the Digital Imaging and Remote Sensing Laboratory at RIT (see http://dirsig.org/index.html). The model can produce passive single-band, multispectral, or hyperspectral imagery from the visible through the electromagnetic spectrum's thermal infrared region.

DIRSIG is a first-principle radiative transfer image and data simulation tool. It generates airborne and satellite imagery through unified path-tracing approaches for light transport. This process generates sensor-reaching radiance from geometric objects and the Earth's surface, attributed with reflectivity and emissivity models. The model can simulate many modalities, including panchromatic; red, green, blue (RGB); multi- and hyperspectral; thermal; polarization; low-light level; light detection and ranging (LIDAR); and synthetic aperture radar. Example imagery of DIRSIG outputs can be seen in Figure 2.

Sensor response functions and noise models enhance the data to produce realistic imagery. Training chips are easily created using the DIRSIG Chip Maker plugin. This plugin simplifies and automates the generation of training images (i.e., various view angles, illumination angles, ground sample distance, etc.). Unlike game engines,

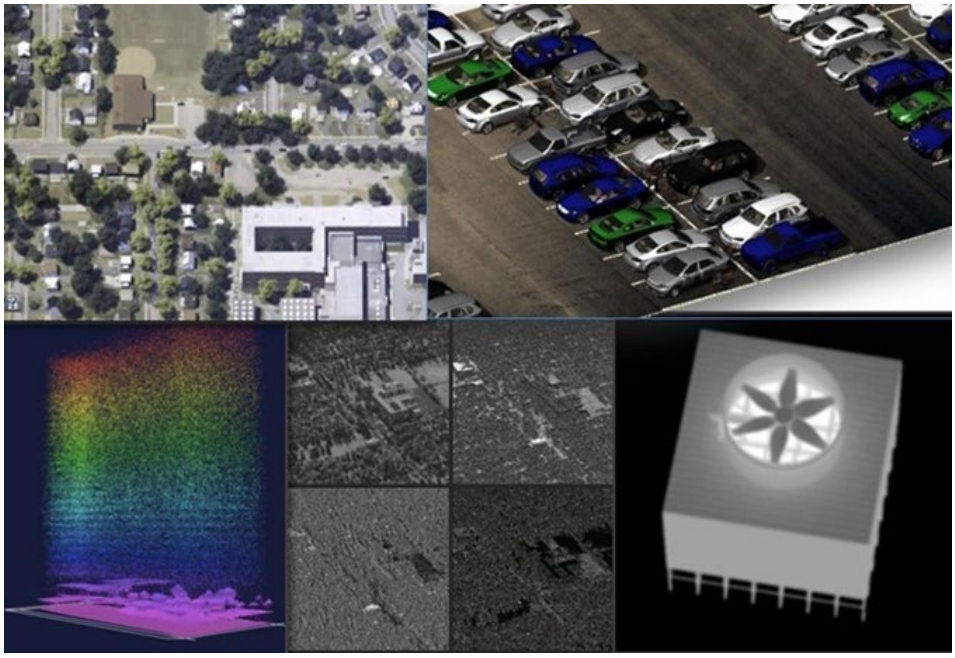

Figure 2: Multimodal Images Generated by the DIRSIG Model: Top Row – (Left) Nadir Hyperspectral and (Right) Oblique RGB; Bottom Row – (Left) LIDAR, (Middle) Polarization, and (Right) Thermal Imagery *(Source: RIT).*

DIRSIG does not drop detail in order to maintain frame rate. Additionally, fine-grain sensor control provides detail for the synthetic sensor. Over the years, DIRSIG has been evaluated in many verification and validation studies [3].

High-Performance Computing (HPC)

DIRSIG requires large computational resources from which the U.S. Air Force ported DIRSIG to an HPC platform [4]. The High Performance Computing Modernization Office (HPCMO) provided HPC systems and expertise to install DIRSIG across U.S. Department of Defense (DoD) systems. The HPCMO offers free HPC access to all DoD civilians, military, and contractors across all the Services. To request access, a DoD Supercomputing Resource Center (DSRC) account needs to be established (by following the directions at https://centers.hpc. mil/users/index.html#accounts). After a DSRC account is established, a user would request to be added to the DIRSIG group by submitting a help desk ticket at https://centers.hpc.mil/users/ index.html#help.

The DIRSIG-HPC has three advantages—processing speed, testing agility, and scene variety. DIRSIG scales across HPC systems easily because DIRSIG 5 now supports multiple cores. A user with DSRC access can render several hundred frames in parallel with DIRSIG 5 using PBS Job Arrays. DIRSIG 5 also includes a Chip Maker module built specifically for training artificial intelligence (AI)/machine-learning (ML) systems. The data generated by DIRSIG can be tailored to match imagery obtained from a particular sensor or satellite platform.

A big advantage of using DIRSIG for AI/ML research results from having perfect truth, as the simulations precisely record what has changed due to the control the geometry of the three-dimensional (3-D) model used to generate the synthetic data. Another reason for using DIRSIG is that we can generate a limitless amount of training data. In our previous work [1, 5], we used DIRSIG-generated pairs of helicopters and backgrounds to train and test our models.

Change Detection With Region Proposal Networks

Our PEARL approach to CD uses *deep learning methodologies* that leverage the strengths of popular network architectures. Deep convolutional neural networks (CNNs) demonstrating breakthrough advances in image classification [6–8] have been used in various applications, including face recognition [9], semantic segmentation [10], object tracking [11], and CD [1, 12]. In our work, we build a simple and scalable model for CD that uses region proposal networks to generate a change map between image pairs. We demonstrate the performance of PEARL on a DIRSIG-generated CD dataset of airplanes.

The PEARL insight utilizes the idea that an image pair of the same location with no major structural changes will have similar object proposals generated in both images. On the other hand, a pair of images with major structural changes (e.g., presence of a plane) will yield different object proposals. After the region proposals provide results for two images, a change map is constructed

Our PEARL approach to CD uses *deep learning methodologies* that leverage the strengths of popular network architectures.

and analyzed to make a change or no-change decision.

The change map highlights arrivals, departures, and deviations. PEARL takes advantage of the proposal information before the final classification stage so that the detected changes are less specific to particular object classes. The initial stages of our investigation show promise of the PEARL method's potential to generalize toward unstructured CD, semistructured activity monitoring, and multimodal transfer learning analysis.

PEARL METHODOLOGY

Siamese networks are promising for CD [1], object tracking [13], and person reidentification [14]. The Siamese models use two identical network channels (with shared weights) to generate feature maps that are further processed for the application of interest. The network channels used for CD in Rahman et al. [1] consist of the convolutional part of pretrained Visual Geometry Group (VGG) object detectors [6]. The VGG features feed a decision network trained to identify changes, as illustrated in Figure 1.

Region Proposal Generation

PEARL utilizes region proposals, which are rectangles identifying the regions of the image most likely to contain objects [15]. Region proposals were incorporated in the Faster R-CNN architecture [8] shown in Figure 3, which is a popular architecture for object detection. Faster R-CNN is a region-based convolutional neural network composed of a feature extractor network, the Region Proposal Network (RPN), and a fully connected network used for detection. The typical feature extractor is a CNN (e.g., ResNet [7]) pretrained on the ImageNet dataset [16].

After receiving the feature maps, the RPN generates a number of bounding boxes, called regions of interest (ROIs), which have a high probability of containing an object. The RPN generates region proposals based on *anchors*, which are boxes of different sizes and aspect ratios. For each window on the feature map, nine anchors based on three different scales and three aspect ratios are generated.

The last stage of the network has a classifier and a regressor. The classifier takes each of the nine anchor boxes for each location and determines if the object belongs to the background or foreground. The regressor predicts four coordinates of a bounding box relative to each anchor. The process generates many proposals for a single image. The RPN then sorts the proposals to find the ones with the highest probability of containing an object. Sorting includes applying nonmax suppression to keep the proposals with the highest confidence.

Nonmax suppression is a method that reduces multiple detections of the same object to just one. It starts with the most confident detection and then looks at all the remaining detection rectangles to determine which ones have significant overlap. The detections with large overlap are suppressed with the assumption that they are generated from the same object. This procedure yields a small number of detections per object. The ROIs produced from the RPN are rectangles of different sizes. However, if their intended use is for further CNN processing, they have to be a predetermined, fixed size. The ROI pooling layer splits the input feature map to a fixed number of equal regions, and max pooling applies to every region.

These fixed feature regions are input into a classifier and regressor. The classifier infers the class and probability of the object belonging to that class. The regressor provides the bounding box coordinates after regression. The objects detected are marked with a bounding box, referred to as *region proposals*.

CD With Region Proposals

Figure 4 presents the CD process. A Faster R-CNN network examines each image pair, consisting of the target

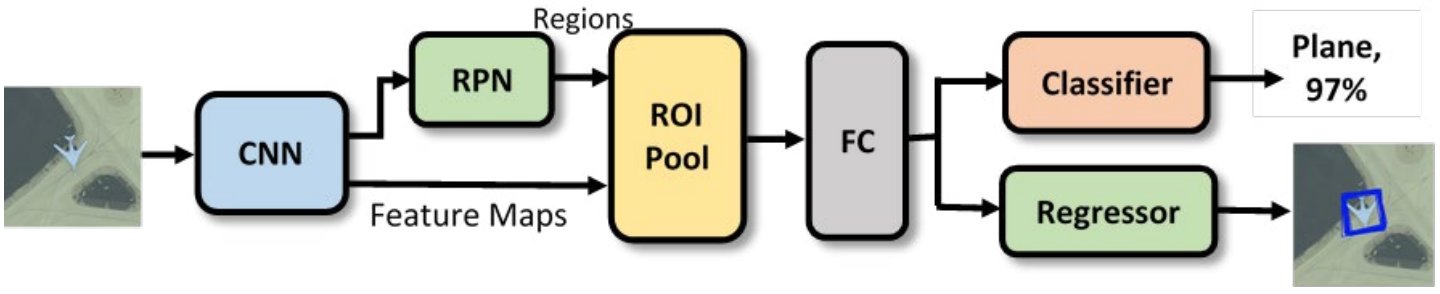

Figure 3: Faster R-CNN Object Detection Network Architecture *(Source: RIT).*

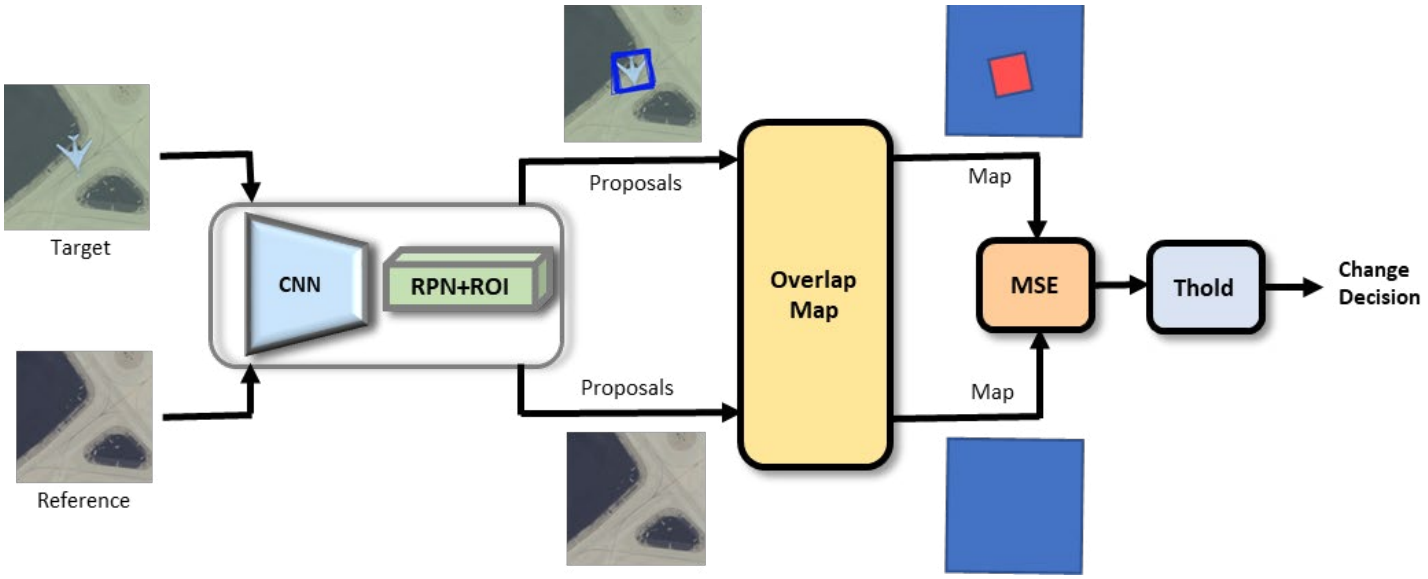

Figure 4: Methodology Used for CD With PEARL *(Source: RIT).*

and reference images, and generates the bounding box coordinates of the proposals. Proposal overlap maps are then created by accumulating the contributions of each region proposal box. The proposal overlap maps provide information of where in the image objects are most likely to exist. These object maps are generated for both the target and reference images in the image pair, which are compared using mean square error (MSE). No-change image pairs have a low MSE, as the same objects are present at the same location in the image pair. Change image pairs have a higher MSE, which indicates a significant structural change between the two images.

EXPERIMENTS AND RESULTS

Training and Testing Datasets

The Faster R-CNN network was originally trained on ImageNet [16], which contains ground-level imagery. However, these types of images are not well suited for remote sensing applications. Since we had to generate a CD map for satellite imagery, we utilized a version of Faster R-CNN [17] trained on the Dataset for Object Detection in Aerial Images (DOTA) [18]. (DOTA is a large-scale dataset for object detection that uses Google Earth images of various locations around the globe.) The DOTA image sizes ranged from 800 x 800 to 4000 x 4000 pixels, with objects in various scales, orientations, and shapes. Annotating the images resulted in 15 object categories, where the most important classes of interest for CD were helicopters, planes, and ships.

The DIRSIG planes dataset was the CD dataset used for testing because DOTA is not a CD dataset and could not be used for testing our method. The planes dataset generated using DIRSIG consisted of scenes with target and reference images measuring 512 x 512 pixels. Different backgrounds and illuminations, with spectral and structural properties similar to commercial satellite imagery, enhanced the dataset. The objects used were four types of planes on different backgrounds and illuminations. The dataset consisted of 1,358 images. Each image had a change and no-change counterpart, making the total number of image pairs 2,716. Representative DIRSIG planes images are shown in Figure 5.

Figure 5: Example Images From the DIRSIG Planes Dataset, With Different Backgrounds and Illuminations *(Source: RIT).*

Annotating the images resulted in 15 object categories, where the most important classes of interest for CD were helicopters, planes, and ships.

Change Detection Results

We applied our CD methodology on the DIRSIG plane's dataset. Examples of the region proposal bounding boxes for change and no-change pairs are shown in Figure 6, where the left, center, and right images represent the original airplane rendering and the background and plane at different illuminations. After contrast stretching the images and applying nonmax suppression, the accuracy of change/no-CD based on the MSE of the overlap maps was 97%. (Note that the changes in illumination did not have a strong effect on generating region proposals.) Additionally, no proposals were generated for the images without planes. These results highlight the advantages of PEARL, including that it is independent of illumination and small changes.

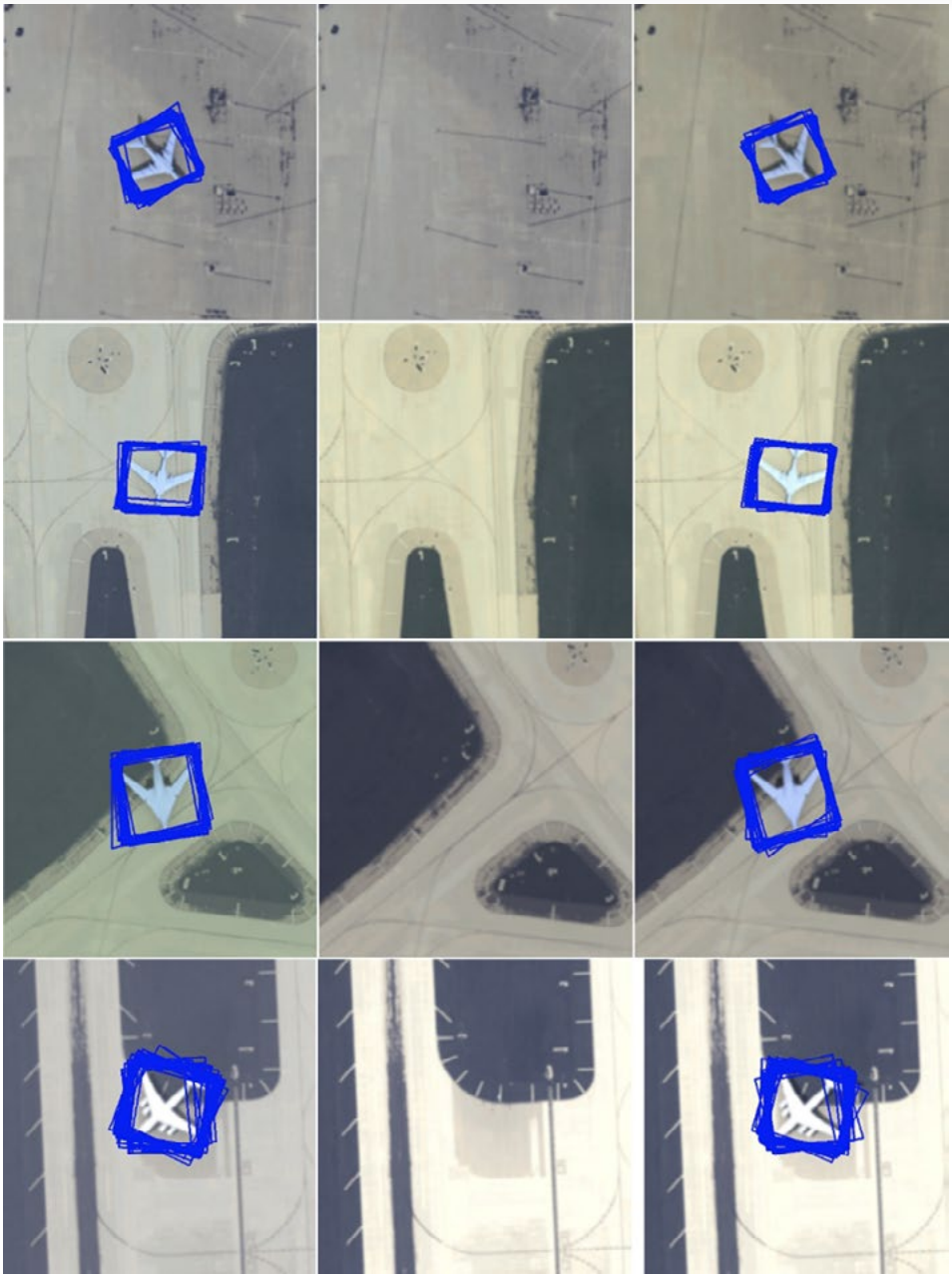

Figure 6. Examples of Change Pairs and Their Generated Region Proposals *(Source: RIT).*

CONCLUSIONS

We presented a new approach for CD in satellite imagery motivated by deep learning architectures for region proposal networks. Our PEARL method had a high success rate in detecting structural changes in the DIRSIG-generated planes dataset. The performance of PEARL was robust to change in illumination and small variations. However, the proposals generated by current networks were influenced by the object types contained in the dataset (e.g., ground-level images in ImageNet vs. satellite images in DOTA). Thus, suitable datasets are still needed for training and testing CD methods. As a result, synthetic dataset generation by DIRSIG was a great value.

ACKNOWLEDGMENTS

This research was funded in part by Kitware Inc., the U.S. Air Force Research Laboratory (AFRL), Air Force Office of Scientific Research (AFOSR), and the Center for Emerging and Innovative Sciences, an Empire State Development-

designated Center for Advanced Technology.

REFERENCES

[1] Rahman, F., B. Vasu, J. Van Cor, J. Kerekes, and A. Savakis. "Siamese Network With Multi-Level Features for Patch-Based Change Detection in Satellite Imagery." Proceedings of the 6th IEEE Global Conference on Signal and Information Processing (GlobalSIP), Anaheim, CA, November 2018.

[2] Goodenough, A., and S. D. Brown. "DIRSIG5: Next-Generation Remote Sensing Data and Image Simulation Framework." *IEEE Journal of Selected Topics in Applied Earth Observations and Remote Sensing*, vol. 10, November 2017.

[3] DIRSIG Verification and Validation Studies." http://www.dirsig.org/docs/new/validation. html, accessed 4 August 2019.

[4] Hardin, D. "Air Force's Newest Supercomputer Supports Game-Changing Research." https://www.wpafb.af.mil/News/Article-Display/Article/819032/air-forces-newest-supercomputer-supports-game-changing-research/, accessed 4 August 2019.

[5] Han, S., A. Fafard, J. Kerekes, M. Gartley, E. Ientilucci, A. Savakis, C. Law, J. Parhan, M. Turek, K. Fieldhouse, and T. Rovito. "Efficient Generation of Image Chips for Training Deep Learning Algorithms." *SPIE Defense and Commercial Sensing, Automatic Target Recognition XXVII*, April 2017.

[6] Simonyan, K., and A. Zisserman. "Very Deep Convolutional Networks for Large-Scale Image Recognition." International Conference on Learning Representations (ICLR), 2015.

[7] He, K., X. Zhang, S. Ren, and J. Sun. "Deep Residual Learning for Image Recognition." *Computer Vision and Pattern Recognition (CVPR)*, 2016.

[8] Ren, S., K. He, R. Girshick, and J. Sun. "Faster R-CNN: Towards Real-Time Object Detection With Region Proposal Networks." *Advances in Neural Information Processing Systems*, 2015.

[9] Schroff, F., D. Kalenichenko, and J. Philbin. "FaceNet: A Unified Embedding for Face Recognition and Clustering." *Computer Vision and Pattern Recognition (CVPR)*, 2015.

[10] Long, J., E. Shelhamer, and T. Darrell. "Fully Convolutional Networks for Semantic Segmentation." *Computer Vision and Pattern Recognition (CVPR)*, 2015.

[11] Minnehan, B., A. Salmin, K. Salva, and A. Savakis. "Benchmarking Deep Learning Trackers on Aerial Videos." *SPIE Defense and Security Symposium, Pattern Recognition and Tracking XXIX*, April 2018.

[12] Daudt, R. C., B. Le Saux, and A. Boulch. "Fully Convolutional Siamese Networks for Change Detection." IEEE International Conference on Image Processing (ICIP), 2018.

[13] Bertinetto, L., J. Valmadre, J. F. Henriques, et al. "Fully-Convolutional Siamese Networks for Object Tracking." Proceedings of the European Conference on Computer Vision (ECCV), pp. 850–865, Springer, 2016.

[14] Chung, D., K. Tahboub, and E. J. Delp. "A Two Stream Siamese Convolutional Neural Network for Person Re-identification." International Conference on Computer Vision (ICCV), 2017.

[15] Yang, F., H. Fan, P. Chu, E. Blasch, and H. Ling. "Clustered Object Detection in Aerial Images." International Conference on Computer Vision (ICCV), 2019.

[16] Deng, J., W. Dong, R. Socher, L. J. Li, K. Li, and L. Fei-Fei. "ImageNet: A Large-Scale Hierarchical Image Database." *Computer Vision and Pattern Recognition (CVPR)*, 2009.

[17] Zhu, Z., and J. Ding. "DOTA Faster R-CNN." https://github.com/jessemelpolio/ Faster_RCNN_for_DOTA, accessed 4 August 2019.

[18] Xia, G. S., et al. "DOTA: A Large-Scale Dataset for Object Detection in Aerial Images." *Computer Vision and Pattern Recognition (CVPR)*, 2018.

BIOGRAPHIES

ANDREAS SAVAKIS is a professor of computer engineering and Director of the Center for Human-aware Artificial Intelligence at RIT. His research interests include computer vision, deep learning, machine learning, and applications. Prior to joining RIT, he was with Kodak Research Labs. He has coauthored over 120 publications and holds 12 U.S. patents. Dr. Savakis received his Ph.D. in electrical and computer engineering from North Carolina State University.

NAVYA NAGANANDA is a research assistant at RIT's Vision and Image Processing Lab under the supervision of Prof. Savakis. Her research interests are in deep learning, image analysis, and machine learning. Ms. Naganandа received her B.S. and M.S. degrees in physics from Indian Institute of Science Education and Research, Thiruvananthapuram, India, and is pursuing her Ph.D. in imaging science at RIT.

JOHN P. KEREKES is a professor in the Chester F. Carlson Center for Imaging Science at RIT. His research interests include remote sensing system analyses and performance sensitivity studies using simulation and modeling techniques. Prior to joining RIT, he was a staff member at the MIT Lincoln Laboratory. Dr. Kerekes received his B.S., M.S., and Ph.D. degrees in electrical engineering from Purdue University.

EMMETT J. IENTILUCCI is an assistant professor at RIT. He has been a program reviewer for the National Aeronautics and Space Administration and the DoD and is Chair for both the Society of Photographic Instrumentation Engineers Imaging Spectrometry Conference and the Western New York IEEE Geoscience and Remote Sensing Society. He has over 65 publications and is currently working on a textbook titled "Radiometry and Radiation Propagation." Dr. Ientilucci received his Ph.D. in imaging science from RIT.

RUSSELL (RUSTY) BLUE is a technical lead in the Computer Vision program at Kitware Inc. His work focuses on leading a team of developers on Kitware's efforts across several government programs in visual content analysis, including the U.S. Air Force Research Laboratory (AFRL) Phase III VIGILANT Small Business Innovation Research (SBIR) and AFRL Do-It-Yourself AI efforts, which both have significant deep learning components. Previously, he developed advanced visualizations in scientific and medical computing based on Kitware's open-source Visualization Toolkit.

WILLIAM HICKS is a senior research and development engineer in the Computer Vision department at Kitware Inc. His work focuses on automated analysis of overhead imagery through the AFRL Phase III VIGILANT SBIR, as well as content-based retrieval across a range of government-sponsored programs.

TODD V. ROVITO is a senior research computer scientist, Decision Science Branch, Multi-Domain Sensing Autonomy Division at AFRL, Wright-Patterson Air Force Base, OH. He works on remote sensing exploitation research and is currently focusing on passive 3-D reconstruction and reasoning and deep learning object detection from commercial space satellite systems.

ERIK BLASCH is a program officer at AFOSR supporting research in dynamic data-driven applications systems. He has been with AFRL as a civilian and reservist since 1996, compiling 700+ scientific papers and 19 patents. He is also the author of multiple books and a SPIE and IEEE Fellow, as well as an AIAA Associate Fellow. Dr. Blasch earned a bachelor's degree in mechanical engineering from MIT; master's degrees in mechanical, health science, and industrial engineering (human factors) from Georgia Tech; and an MBA, master's degrees in electronics and economics, and Ph.D. in electrical engineering from Wright State University. He is also a graduate of the Air War College.

(Photo Source: 123rf.com)

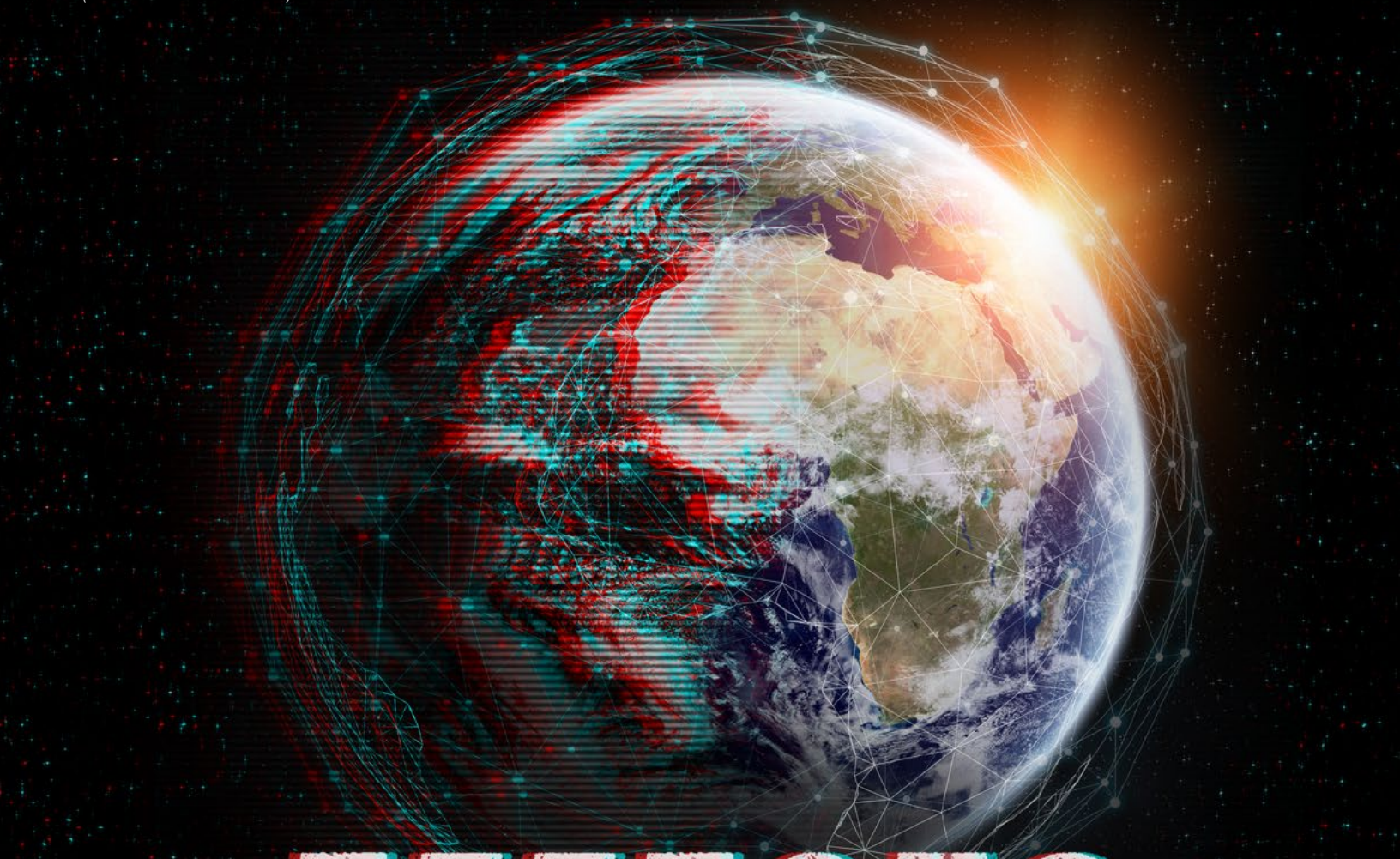

EFFECTS of Material Properties on ISR for Synthetic Aperture Radar

By Qaisar Manzoor

SUMMARY

This research looks at the various factors that affect image appearance of a target in microwave and radar frequencies. To better understand how to implement unconventional countermeasures, it is important to understand the physical and material properties that affect target detection, recognition, and identification in intelligence, surveillance, and reconnaissance (ISR) missions. The research was conducted through a basic understanding of material properties and electromagnetic radiation. A deeper understanding of the material properties—to include atomic structures of materials, dipole moment, polarization, and permittivity—is also discussed. Current research has shown that the relative permittivity of a material plays a significant role in how that material interacts with certain electromagnetic radiation; thus, the various factors affecting permittivity are also discussed. This research attempts to identify material property characteristics that can be introduced into models that will lead to a better understanding of the image appearances of targets in microwave and radar frequencies.

INTRODUCTION

Synthetic aperture radar (SAR) was developed in the 1950s as a tool for the U.S. Army to conduct 24-hour surveillance in all weather conditions. SAR's ability to penetrate clouds and fog made it a naturally effective surveillance tool. Modern SAR systems utilize computer processing to detect and recognize target signatures in collected data. SAR operates in the radio and microwave regions of the electromagnetic (EM) spectrum [1]. A depiction of EM frequency ranges is shown in Figure 1.

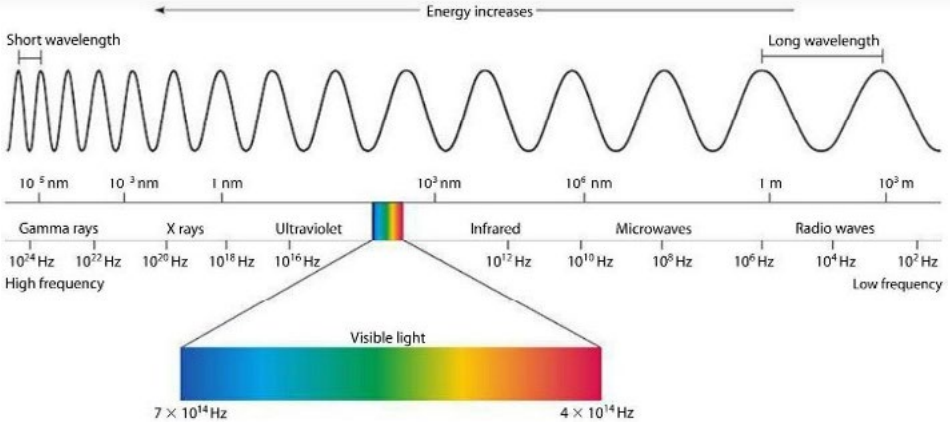

Figure 1: EM Spectrum *(Source: The Electromagnetic Spectrum [1]).*

SAR transmits and receives EM waves used to build an image of the expected target area. The SAR "aperture" refers to the radar system antenna that receives the EM signal. In general, a radar image is better resolved with a larger antenna aperture. However, in remote sensing applications, a large aperture is generally not feasible. SAR overcomes this limitation by utilizing the motion of the sensor platform relative to the target to artificially create a larger simulated aperture. In remote sensing applications, the motion-based aperture is typically created by the motion of an aircraft or satellite system. Figure 2 shows a schematic of how SAR acquires imagery.

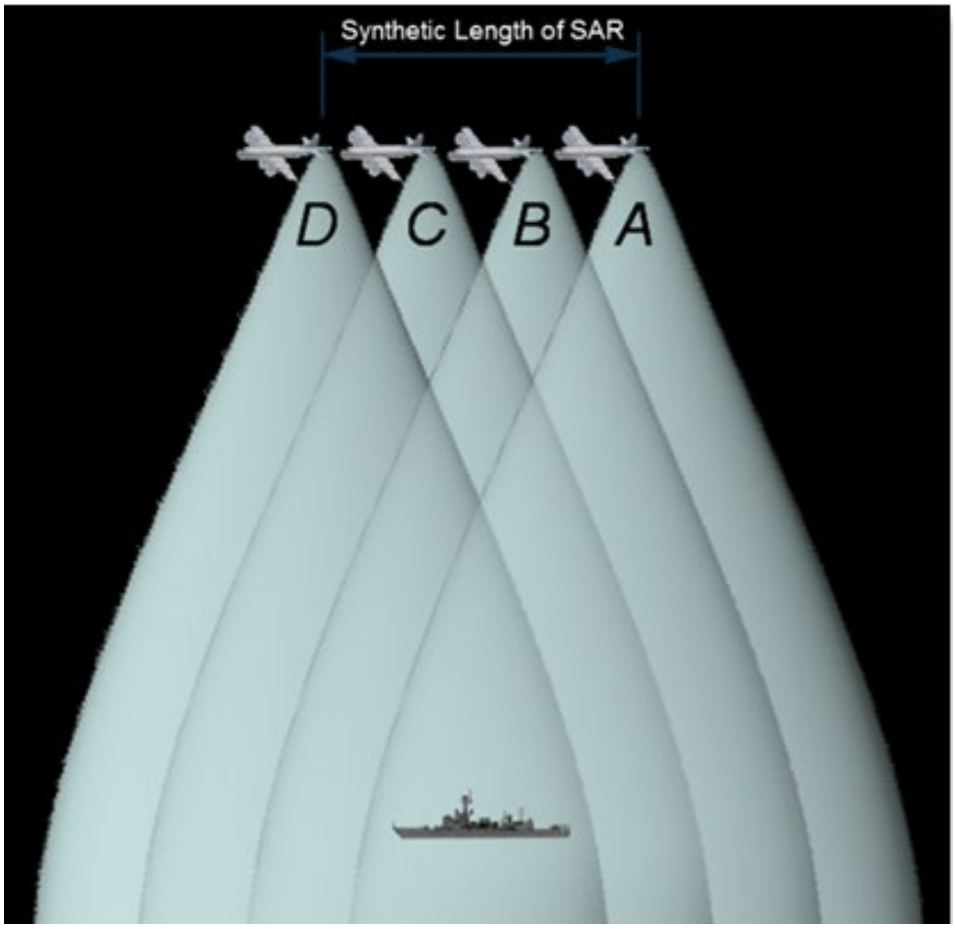

Figure 2: Example of SAR Collection From Airborne Asset *(Source: Wolff [2]).*

FACTORS AFFECTING SAR

SAR can provide images day and night and penetrate dust, fog, smoke, and other atmospheric obstructions [3]. This versatile capability provides target imagery in conditions where other electromagnetic sensors, such as visual and infrared (IR), are precluded. SAR operates by transmitting EM waves toward a target and receiving the waves reflected back to the receiver. Factors that affect radar return from the target include surface roughness, radar viewing angle and surface geometry, and material properties of the target [3]. The temperature of a material also has an effect on the way an object of a certain material type or composite of materials will appear in SAR imagery [4]. As the temperature increases, polarization of the material decreases; thus, the dielectric constant of the material decreases. More energy is required from the incoming electromagnetic waves to polarize the material, which

means more energy is absorbed, less energy is reflected, and the material has a darker tone in SAR imagery. On the atomic level, polarization and dipole moment of the material have a sizable effect on SAR signatures within a scene [5].

Surface Roughness

Figure 3a depicts surface roughness, which is determined by the incident angle of the incoming EM wave and its wavelength [6]. For a smooth surface, the relationship between the incident angle and the wavelength is given by the Fraunhofer criterion $\Delta h < (\frac{\lambda}{32Cos\theta})$ or the Rayleigh criteria $\Delta h < \left(\frac{\lambda}{8Cos\theta}\right)$ [7]. A smooth surface will have specular reflection (i.e., most of the EM waves will be reflected away from the radar receiver). Such a surface will appear as a dark tone in a radar image.

A rough surface is one that does not meet the Fraunhofer criterion or Rayleigh criteria and will cause diffuse reflection of the incoming waves. Diffuse reflection causes the EM waves to reflect in all directions, which means more of the transmitted waves return to the radar receiver. This results in a brighter tone of the target relative to its surroundings in the radar image.

Corner reflections occur when man-made or natural features have two or more surfaces (usually smooth) at right angles to each other and the corner faces in the general direction of the radar antenna. This right angle surface orientation causes most of the transmitted waves to reflect directly back to the antenna due to double or multipath reflections, which results in brighter targets in radar images [6]. Some examples of corner reflection are buildings, streets, bridges, cliff faces, and upright vegetation standing in water [8].

Diffuse reflection causes the EM waves to reflect in all directions.

Radar Viewing Angle and Surface Geometry

Figure 3b shows radar viewing and surface geometry that account for the local incident angle (A), which is the angle between the EM wave and a line perpendicular to the slope at the point of incidence, and the look angle (B), which is the angle between the vertical plane passing through the radar antenna and the line between the antenna and target. If A is equal to B, then the resulting reflection is specular, resulting in darker image tones. For slopes facing toward the radar, if A is not equal to B, the reflected waves are strongly backscattered, resulting in a bright image tone.

The orientation of the transmitted radar beam relative to the direction or alignment of linear features on the surface is described by the look direction and depicted in Figure 3c. A nearly perpendicular orientation of the look direction to the feature (shown by look direction angle A) will cause a large portion of the incident wave to reflect back to the sensor, and the feature will appear brighter. An oblique orientation of the look direction to the feature (shown by look direction angle B) will cause a small portion of the incident wave to reflect to the radar, and the feature will appear darker in tone [6].

Material Properties

Target material properties play a major role in that target's SAR imagery. These properties include relative permittivity (dielectric constant) and permeability of the material. Absolute permittivity of the material describes the resistance of a material to set up an internal electric field in the material in the presence of an external electric field. Relative permittivity is the permittivity of a

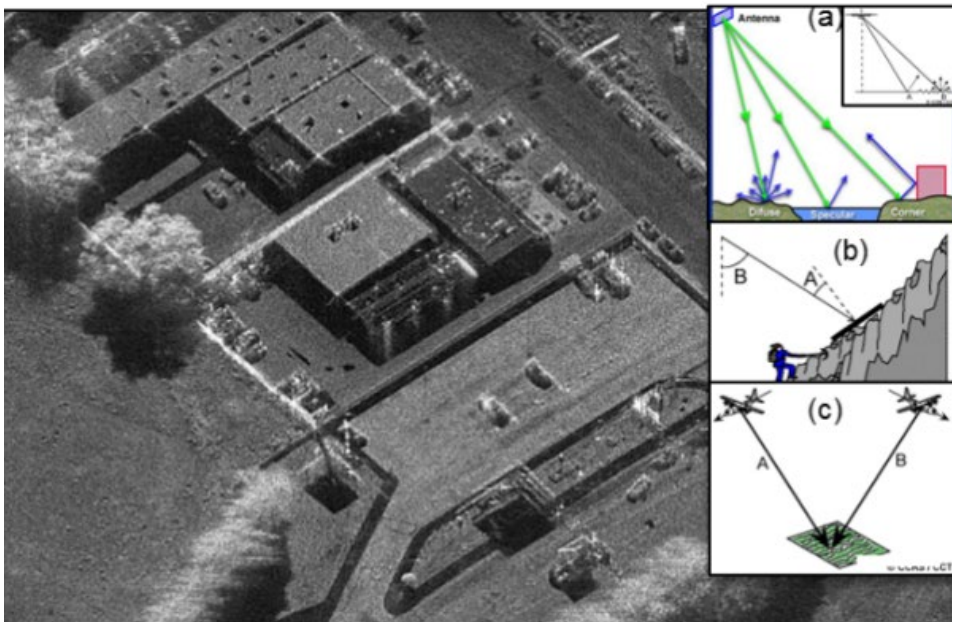

Figure 3: Effects of (a) Surface Roughness, (b) Viewing Angle and Surface Geometry, and (c) Orientation *(Sources: Natural Resources Canada [6] and Charvat [9]).*

material relative to the permittivity of a vacuum (ε_r) [10]. Permeability describes the ability of a material to support the formation of a magnetic field inside the material. Along with these intrinsic properties, the thickness of the material, the radar frequency, and the transmitted wave's incident angle greatly affect how the material appears in SAR imagery [11]. Together, these factors define the complex refractive index and absorption loss that an incoming wave will experience as it propagates through the material.

The Fresnel equations shown in Table 1 define the ratio of the reflected wave and the transmitted wave to the incident wave for the perpendicular and parallel components of the electric field. These equations utilize the complex refractive index given by (1) $\tilde{n} = n + ik$, where $\tilde{n}$ is the complex refractive index determined by the material refractive index $n = \sqrt{\varepsilon_r \mu_r}$, and (2) absorption loss (also known as extinction coefficient) $= 8.7\left(\frac{t}{\delta}\right)$, where $\delta = \frac{1}{\sqrt{(\pi f \varepsilon_r \mu_r)}}$ and determines the ratio of the reflected waves from an object and transmitted waves through the object. The material relative permittivity (ε_r), relative permeability (μ_r), and frequency of the incoming electromagnetic radiation (f) affect the refractive material index, which affects the reflected and transmitted radiation according to the Fresnel equations [12]. The effects of these factors define how much of the incident wave is reflected back to the radar, which determines how bright or dark the target appears compared to its surroundings.

Table 1: Fresnel Equations

PERPENDICULAR E FIELD VECTOR	PARALLEL E FIELD VECTOR
$\frac{E_r}{E_i} = \frac{n_1 cos\theta_1 - n_2 \cos\theta_2}{n_1 \cos\theta_1 + n_2 \cos\theta_2}$	$\frac{E_r}{E_i} = \frac{n_2 cos\theta_1 - n_2 cos\theta_2}{n_1 \cos\theta_2 + n_2 \cos\theta_1}$
$\frac{E_t}{E_i} = \frac{2n_1 \cos\theta_1}{n_1 \cos\theta_1 + n_2 \cos\theta_2}$	$\frac{E_t}{E_i} = \frac{2\, n_{1 \cos\theta_1}}{n_1 \cos\theta_2 + n_2 \cos\theta_1}$

PROPERTIES

Material Bond Types

At the atomic level, the type of chemical bonds in a material affects polarization and dipole moment, which, in turn, affects the material's relative permittivity. Relative permittivity and permeability have a great effect on the complex refractive index of a material. Polar bonds form between two nonmetallic elements and have molecules with large dipole moments (e.g., hydrochloric acid [HCL] and water [H_2O]). Nonpolar bonds form between two nonmetallic elements and have molecules with very small or no dipole moments (e.g., carbon dioxide [CO_2] and methane [CH_4] [13]). Ionic bonds form between metals and nonmetals (e.g., sodium bromide [NaCl] and calcium chloride [$CaCl_2$] [14]). Metallic bonds occur between atoms of a metal. Attraction between one atom's nucleus and a neighboring atom's electrons packs the atoms closely together. This arrangement allows electrons to move freely from one atom to another. This subsequently makes metals good conductors, as they possess free-flowing electrons. Figure 4 shows the general arrangements of atoms and/or molecules in solids, liquids, and gases [15].

Relative permittivity and permeability have a great effect on the complex refractive index of a material.

4.2 Polarization

Polarization expresses the density of permanent or induced electric dipole moments in a dielectric material [17]. When an external electric field is applied to a material, it causes a displacement of bound, charged elements. These elements are not free to move about

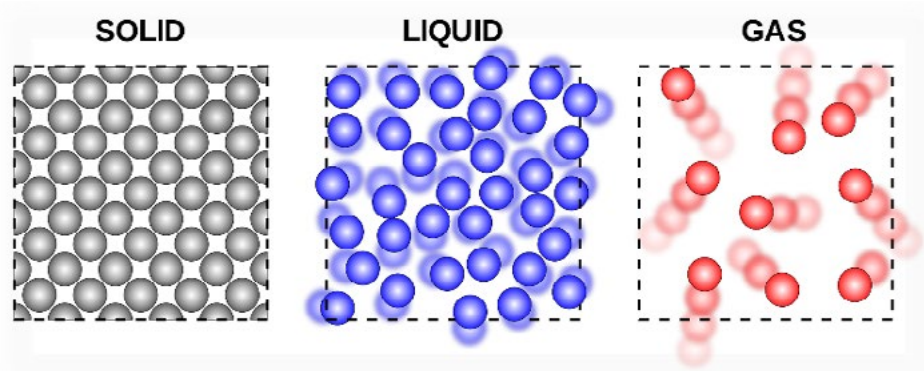

Figure 4: Example of Atomic Distribution in Solids, Liquids, and Gases *(Source: Wikipedia [16]).*

the material. As a result, the positively charged elements are displaced in the direction of the applied electric field, while the negatively charged elements are displaced opposite the direction of the applied electric field. The molecule as a whole may remain neutral in charge, yet an electric dipole moment is formed. So a stronger dipole moment results in a stronger molecular resistance to rotation, and, hence, more energy is required to rotate the molecules. Such a material would absorb much more energy. Figure 5 shows different stages of polarization in a material [18].

Permittivity

The effect an applied electric field on a material is described by its permittivity. Higher permittivity tends to reduce any electric field set up in the material. The relative permittivity (dielectric constant) of a material is the ratio of the permittivity of the material to the permittivity of a vacuum. A material will have a greater dielectric constant with greater polarization developed in the material [20].

TYPES OF POLARIZATION

Electronic Polarization

Electronic polarization occurs when a neutral atom is subjected to an external electric field. The charges are redistributed, and the electrons shift from equilibrium with respect to the positive nuclei. This reorientation results in an induced dipole moment. In crystalline elements comprised of covalent (molecular) bonds, the valence electrons in these bonds are easily shifted compared to the rigid ionic cores when subjected to an external electric field. This type of polarization is responsible for large dielectric constants, such as silicon with a relative permittivity of 11.9 and germanium with a relative permittivity of 16 [18].

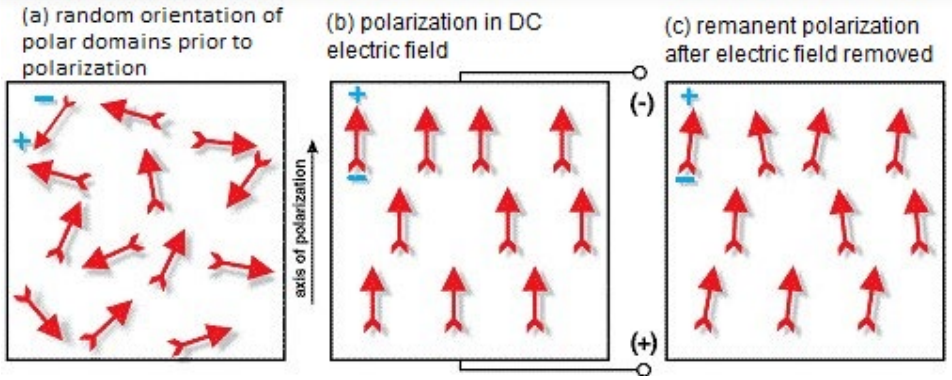

Figure 5: Atomic/Molecular Polarization in Response to External EM Field *(Source: Asztalos [19]).*

Atomic or Ionic Polarization

Atomic or ionic polarization is due to the relative displacements of the atoms or ions within molecules and crystal structures from their equilibrium states. Examples of atomic or ionic polarization include potassium fluoride (KF) and potassium chloride (KCl) [18].

Orientation or Dipolar Polarization

Orientation or dipolar polarization occurs in materials with molecules that contain permanent dipole moments, such as water and hydrogen chloride. When no external electric field is applied to such materials, the molecules are randomly oriented due to thermal activation. This produces no net dipole moment. In the presence of an applied external electric field, random (polar) molecules with permanent dipoles try to align parallel to the electric field. Under certain frequencies, the dipoles respond to the alternating electric field by rotating to align with the external electric field. The dipoles are unable to align themselves with the external electric field in sufficient time, creating a phase difference between the orientation of the electric field and the dipoles. This phase difference causes molecular collisions and releases energy in the form of dielectric heating [18].

Orientation or dipolar polarization occurs in materials with molecules that contain permanent dipole moments.

Interfacial (Maxwell-Wagner) Polarization

Interfacial (Maxwell-Wagner) polarization, also known as space charge polarization, is due to the accumulation of free charges at interfaces located within the material or between different materials. In the absence of an external electric field, the material has equal numbers of positive and negative ions; therefore, there are no charge separations between the opposing ions. Mobile charges accumulate at barriers, such as grain/phase boundaries, or at free surfaces in the presence of an external electric field. This results in interfacial polarization. Figure 6 depicts the different kinds of polarization as described in Gupta and Wong Wai Leong [18].

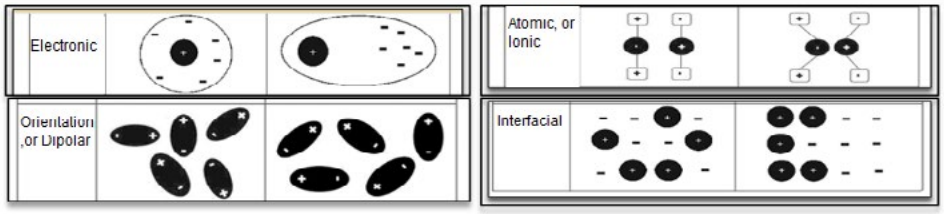

Figure 6: Types of Polarization *(Source: Gupta and Wong Wai Leong [18]).*

FREQUENCY DEPENDENCE OF POLARIZATION

Polarization is frequency dependent. Due to their small mass, electrons have little inertia and can follow the alternating electric fields up to high frequencies in the visible light portion of the EM spectrum. Electronic polarization can occur almost in phase with an electromagnetic field and does not generally contribute to microwave absorption by the material. Atomic or ionic polarization is dependent on available thermal energy. This energy corresponds to frequencies in the IR region. Such polarization can also occur in phase with the electromagnetic field and does not generally contribute to microwave absorption. Orientation or dipolar polarization occurs near the radio-to-microwave frequencies due to the considerable mass of molecules with permanent dipole moments, such as water. Interfacial polarization occurs due to the movement and accumulation of charges across the body of a material, so the process occurs at much lower frequencies. Therefore, processing dielectric materials using microwaves depends primarily on dipolar and interfacial polarization. Figure 7 shows the frequency dependence of the different types of polarization [18].

TEMPERATURE DEPENDENCE ON POLARIZATION

Temperature influences a material's polarization. Molecules have some energy that produces random molecular motion. Because there is an equivalent amount of random motion in all directions, the net molecular motion is neutral. When a material with polar molecules is subjected to an external electric field, the molecules will try to align themselves in the direction of the applied electric field. However, if the material temperature is raised, the internal molecular motion increases, and the alignment with the applied electric field becomes more difficult. The orientational polarization is less, so the dielectric constant is also less [5].

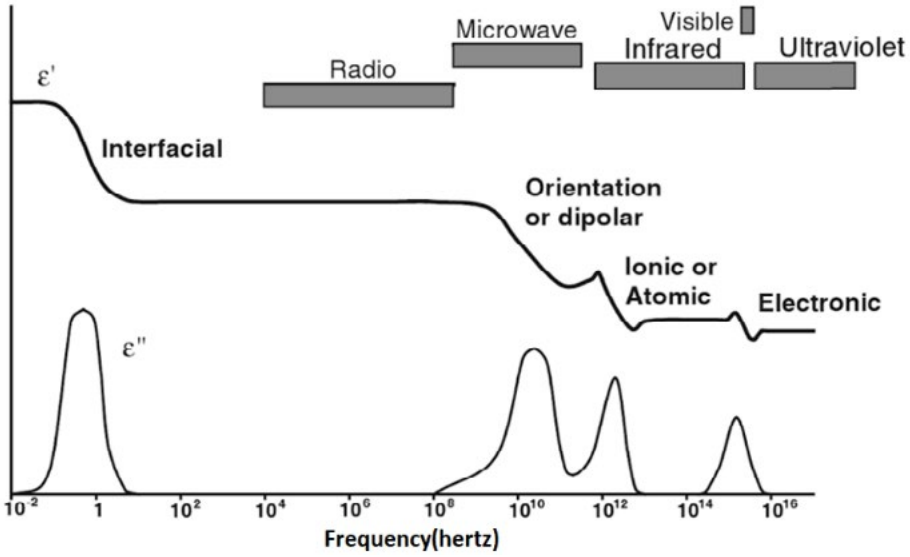

Figure 7: Frequency-Dependent Polarization *(Source: Gupta and Wong Wai Leong [18]).*

Processing dielectric materials using microwaves depends primarily on dipolar and interfacial polarization.

CONCLUSIONS

Intrinsic material properties play a major role in how those materials appear in SAR imagery. Since the properties are inherent to all natural materials, it becomes important to understand not only the reactions of material to certain frequencies but also the electrophysical driving forces in play. The relative roughness or smoothness of a surface has a major effect on SAR appearance when considering EM wavelength. The temperature of the interrogated material is another important consideration because as temperature increases, the dielectric constant (relative permittivity) *decreases*. As the permittivity (resistance to setting up an electric field) increases, the dielectric constant *increases*. Molecular polarization affects EM energy absorption and, thus,

its measured SAR return. As this article demonstrates, great care must be taken to account for all of these material properties and their influence on SAR imagery data. ■

ACKNOWLEDGMENTS

The author thanks Dr. Steven Price, Associate Professor, Mississippi College, Electrical Engineering, and Mr. Clay Blount, Research Chemical Engineer, Survivability Engineering Branch, Geotechnical and Structures Laboratory (GSL), U.S. Army Engineer Research and Development Center (ERDC), for their review and helpful comments on earlier drafts of this article.

REFERENCES

[1] Mini Physics. "The Electromagnetic Spectrum." https://www.miniphysics.com/electromagnetic-spectrum_25.html, accessed July 2019.

[2] Wolff, C. "Radar Basics." http://www.radartutorial.eu/20.airborne/ab07.en.html, accessed July 2019.

[3] Radar and Electromagnetic Spectrum. "Types of Images." http://slideplayer.com/slide/4403225/ 14/images/12/Radar+and+the+Electromagnetic+Spectrum.jpg, accessed 17 September 2018.

[4] Al-Ghamdi, A. A., O. A. Al-Hartomy, F. R. Al-Solamy, N. Dishovsky, D. Zaimova, R. Shtarkova, and V. Iliev. Scientific Research. "Some Factors Influencing the Dielectric Properties of Natural Rubber Composites Containing Different Carbon Nanostructures." https://www.scirp.org/journal/PaperInformation.aspx?PaperID=64056, accessed 12 October 2018.

[5] University of Cambridge. "Effect of Temperature on the Dielectric Constant." https://www.doitpoms.ac.uk/tlplib/dielectrics/temperature.php, accessed 18 October 2018.

[6] Natural Resources Canada. "Target Interaction and Image Appearance." https://www.nrcan.gc.ca/node/9311, accessed 22 October 2018.

[7] Papathanassiou, H. K. Earth Online. "Rough Surface Scattering Models," https://earth.esa.int/documents/653194/656796/Rough_Surface_Scattering_Models.pdf, accessed 23 October 2018.

[8] Earth Online. "Radar Course 2." https://earth.esa.int/ web/guest/missions/esa-operational-eo-missions/ers/instruments/sar/applications/radar-courses/content-2/-/asset_publisher/qIBc6NYRXfnG/ content/radar-course-2-parameters-affecting-radar-backscatter, accessed 6 November 2018.

[9] Charvat, G. L. "Radar Imaging in Your Garage: Synthetic Aperture Radar." https://hackaday.com/2014/03/17/radar-imaging-in-your-garage-synthetic-aperture-radar/, 17 March 2014.

[10] electronicsnotes. "Dielectric Constant & Relative Permittivity." https://www.electronics-notes.com/articles/basic_concepts/capacitance/dielectric-constant-relative-permittivity.php, accessed 6 November 2018.

[11] Wikipedia. "Permeability (Electromagnetism)." https://en.wikipedia.org/wiki/Permeability_ (electromagnetism), accessed 6 November 2018.

[12] Learn EMC. "Shielding Theory." https://learnemc.com/shielding-theory, accessed 5 December 2018.

[13] Chemistry 301: University of Texas. "Polar Bonds." https://ch301.cm.utexas.edu/section2.php?target=imfs/polar/polarbonds-all.php, accessed 5 December 2018.

[14] Schneider, H. J. "Ionic Interactions in Supramolecular Complexes." In *Ionic Interactions in Natural and Synthetic Macromolecules*, edited by A. Ciferri and A. Perico, Wiley Online Library, 2012, https://onlinelibrary.wiley.com/ doi/abs/10.1002/9781118165850.ch2, accessed 11 February 2019.

[15] Clark, J. Chemistry LibreTexts. "Metallic Bonding," https://chem.libretexts.org/Bookshelves/Physical_and_Theoretical_Chemistry_Textbook_Maps/Supplemental_Modules_(Physical_and_Theoretical_Chemistry)/Chemical_Bonding/Fundamentals_of_Chemical_Bonding/Metallic_Bonding, accessed 11 February 2019.

[16] Wikipedia. "Fluid Mechanics for Mechanical Engineers/Introduction." https://en.wikiversity. org/wiki/Fluid_Mechanics_for_Mechanical_Engineers/Introduction, 15 May 2019.

[17] Wikipedia. "Polarization Density." https://en.wikipedia.org/wiki/Polarization_density, accessed 11 February 2019.

[18] Gupta, M., and E. Wong Wai Leong. "Introduction to Microwaves. In *Microwaves and Metals*, Singapore: John Wiley & Sons (Asia) Pte Ltd., 2007, https://books. google.com/books?id=nx6N4dq7zJgC&pg=PA38&lpg=PA38&dq=calculate+frequency+dependent+conduction+loss+in+materials&source=bl&ots=xrpKzUmoD6&sig=DiKCZe7LdtAPWYoBQzZ66VS85IA&hl=en&sa=X&ved=0ahUKEwjptc6hhLrYAhUPON8KHQM3CSIQ6AEIYDAJ#v=onepage&q=calculate%20frequency%20dependent%20conduction%20loss%20in%20materials&f=true, accessed 19 February 2019.

[19] Asztalos, K. "Design and Development of a Nasal Inhaler." Armour College of Engineering, Illinois Institute of Technology, https://www.researchgate.net/ publication/317701554_Design_and_Development_of_a_Nasal_Inhaler, 29 April 2016.

[20] University of Cambridge. "The Dielectric Constant." https://www.doitpoms.ac.uk/tlplib/dielectrics/dielectric_constant.php, accessed 19 February 2019.

BIOGRAPHY

QAISAR MANZOOR is a member of the Unconventional Countermeasures team at GSL, ERDC. His research focuses on understanding the interactions between electromagnetic radiation and material properties on SAR, IR, and multispectral imaging. As a veteran of the U.S. Armed Forces, he served in the U.S. Navy, Army, and Army Reserve. Mr. Manzoor completed his B.S. in physics, with a second major in mathematics from The University of Memphis. He is currently pursuing his master's degree in applied physics from Johns Hopkins University, MD.

THE GREEN MONOPROPELLANT:

Developing and Flight Testing AF-M315E, a Hydrazine Replacement

By Nicholas Keim, Alexander Bishop, Benjamin Hill-Lam, and Benjamin Schwantes

INTRODUCTION

Hydrazine has been the go-to propellant for spacecraft and satellites for more than half a century. While effective and proven, its use comes with many hazards. Researchers are currently developing and testing a new generation of green propellants that will eventually replace hydrazine for space propulsion applications.

HYDRAZINE—THE ORIGINAL MONOPROPELLANT

Hydrazine, chemical composition N_2H_4, is a colorless liquid used in many propulsion applications. Hydrazine and its derivatives have been associated with the rocket community for over 80 years and used for propulsion, control, and power generation purposes. It continues to be used as a monopropellant (passed

(Photo Source: 123rf.com)

over a catalyst, decomposed into hot gaseous products, and exhausted through a nozzle), mainly in satellite control operations and as a bipropellant (generally combined with a hypergolic oxidizer, causing combustion with gaseous products expanded out of the nozzle) for spacecraft propulsion.

Hydrazine was first developed as a hypergolic propellant by the Germans for the Me 163 rocket plane in 1937. They combined "C-Stoff," a mixture of 30% hydrazine hydrate, 57% methanol, and 13% water, with hydrogen peroxide (H_2O_2) to achieve a hypergolic reaction. Since then, hydrazine and its derivatives, such as unsymmetrical dimethyl hydrazine (UDMH – $H_2NN(CH_3)_2$) and monomethyl hydrazine (MMH – $CH_3(NH)NH_2$), have found widespread use in both hypergolic systems for high-impulse, propulsion applications. The Viking orbiters of the late 1970s used a hypergolic combination of MMH and nitrogen tetroxide for propulsion. The Mars Phoenix Lander used hydrazine retrorockets for its descent to Mars. The TITAN-II and TITAN-III missile systems used a hypergolic combination of hydrazine and dinitrogen tetroxide for their main propulsion systems on both the first and second stages (Figure 1) [1].

The first use of hydrazine as a monopropellant was demonstrated by the National Aeronautical and Space Administration (NASA) Jet Propulsion Lab in Pasadena, CA, in 1954. The development of Shell Catalyst 405, which allowed extended reusability and restartability of a hydrazine-based propulsion system, marked a true breakthrough in the use of hydrazine as a monopropellant. As a monopropellant, hydrazine continues to see considerable use in commercial satellites and low-impulse applications, such as the Iridium Satellite Constellation. This application provides altitude control and orbit maintenance coverage to satellite phones due to the reliability of its decomposition reaction with a catalyst and its long development and heritage [3].

A long development history and flight heritage continue to make low-risk, hydrazine-based propulsion systems attractive for mission designers.

Benefits of Hydrazine

Hydrazine has a multitude of benefits as a propellant, especially in altitude maintenance and attitude adjustment on satellites and spacecraft. Its relatively low decomposition temperature and the high-pressure gas generated during decomposition make it ideal as a monopropellant for spacecraft position control. Prior to hydrazine, satellite altitude control was implemented with high-pressure gas (cold nitrogen), which provided a very low impulse and had a number of other problems such as long-term storage and leakage issues through the valves. Hydrazine solved these issues while improving performance; it could be stored as a liquid at low pressure, in a lower-volume tank, and with better sealing in the valves. It also provided higher performance through its decomposition than any cold gas system could achieve [4]. Because hydrazine does not undergo long-term chemical changes in storage (provided that material compatibility is observed), it allows a robust supply of propellant to conduct maneuvers for the satellite's lifetime. A long development history and flight heritage continue to make low-risk, hydrazine-based propulsion systems attractive for mission designers, despite the hazards associated with the chemical.

Figure 1: Titan II Launch Using a Hydrazine-Based Propulsion System *(Source: Maj. Dan Wetmore, U.S. Air Force [2]).*

Problems and Dangers of Hydrazine

Despite its many benefits for spacecraft propulsion, hydrazine is a dangerous substance, especially during ground operations. It is toxic to humans, which necessitates extreme care in handling during satellite or spacecraft loading operations, thus driving up costs. The safety data sheet for hydrazine lists many potential health effects, such as irreversible eye injury, temporary blindness, allergic reaction with the skin, severe burns and ulceration, and liver kidney damage, chemical pneumonitis, and pulmonary edema if inhaled. It has also proved to be a carcinogen for animals; however, this carcinogenic nature has not been verified in humans. Absorption through the skin may cause death [5]. These toxicities necessitate using Self-Contained Atmospheric Protective Ensemble (SCAPE) suits when handling hydrazine to prevent any possible bodily exposure to the fuel or its fumes (Figure 2).

The second most concerning problem with hydrazine is its strong reducing-agent properties. Upon exposure to air, a porous material, or a small amount of heat, hydrazine can spontaneously decompose. These properties make hydrazine attractive as a monopropellant (low energy required to induce decomposition) but extremely dangerous for humans. Its reaction to air means it must be kept under a nitrogen blanket to prevent exposure to oxygen. It can corrode metals, leading to tank leakage and fuel contamination. Though common metals like 304 stainless steel and aluminum 1100 show good compatibility, care must be taken to ensure that the hydrazine does not come into contact with incompatible materials. Iron, nickel, brass, bronze, and copper all show poor compatibility with hydrazine. Hydrazine can also absorb carbon dioxide from the environment, causing it to become more corrosive and accelerating its decomposition rate [7].

The overall cost and difficulty of handling hydrazine have made developing alternative green fuels a priority for the propulsion community.

Due to its long use as a propellant, many effective risk mitigation techniques have been developed to ensure operational safety when dealing with hydrazine; however, the overall cost and difficulty of handling hydrazine have made developing alternative green fuels a priority for the propulsion community.

Green Alternatives to Hydrazine

Although hydrazine is a remarkable chemical, the challenges associated with handling it and the true hazard it poses in the event of human exposure have driven a search for a more benign alternative that meets or exceeds the performance of hydrazine as a monopropellant. The term “green monopropellant” encompasses a reduction in overall handling and safety requirements—low toxicity, noncarcinogenic, noncorrosive, low vapor pressure to reduce exposure routes and flammable headspace, no requirement for SCAPE suits when handling, and transportability by commercial aircraft.

The 2006 European Union (EU) Regulation (EC) No. 1907/2006 requires all chemical substances produced or used by industry to be registered with the European Chemicals Agency (ECHA) [8]. Substances of very high concern (SVHC) are given a sunset date after which the manufacture, import, and use of the substance in the EU will be prohibited unless specific authorization is granted by ECHA. Hydrazine was

Figure 2: Members of a Hydrazine Response Team Use Protection to Prevent a Simulated Hydrazine Leak From Spreading *(Source: Tech. Sgt. Christopher Stewart, National Guard [6]).*

added to the candidate list of SVHCs in 2011; while no sunset date has been assigned, it is clear to industry that hydrazine will need to be replaced in order to comply with EU regulations.

For all green monopropellants, the strategy for achieving the safety goals is generating ternary ionic solutions based on an oxidizing salt and fuel mixture with water. Common oxidizing salts are hydroxylammonium nitrates (HANs), ammonium dinitramide (ADN), hydrazinium nitroformate (HNF), and ammonium nitrate (AN) [9].

The European search for a hydrazine replacement began in earnest in 2008 with a project called Green Advanced Space Propulsion (GRASP), a consortium of 12 universities and organizations led by the University of Applied Sciences Wiener Neustadt [10]. The GRASP program identified a number of possible hydrazine replacements, including some already well into their development, such as FLP-106 and LMP-103S. Both of these propellants are based on ADN, a strong oxidizer originally discovered at the Zelinsky Institute of Organic Chemistry in Moscow, USSR, in 1971. ADN remained a state secret until it was rediscovered in 1988 by researchers at Stanford Research Institute in the United States [11].

FLP-106 and LMP-103S have been in development since the late 1990s by Totalförsvarets forskningsinstitut, the Swedish Defense Research Agency (FLP-106), and commercial firm Ecological Advanced Propulsion Systems (LMP-103S), both collaborating with the Swedish Space Corporation [12]. These propellants, which have demonstrated low toxicity and high performance, are viable candidates for replacing hydrazine for monopropellant space propulsion systems [13]. LMP-103S has been flight tested on the Prisma satellite launched in 2010 and demonstrated 2.3 hours of accumulated firing time through the summer of 2011 [14].

The United States began the Integrated High Payoff Rocket Propulsion Technology Program to drive large improvements in the state of propulsion technology for the DoD and NASA.

In 1993, the United States began the Integrated High Payoff Rocket Propulsion Technology Program to drive large improvements in the state of propulsion technology for the U.S. Department of Defense (DoD) and NASA [15]. Goals for improving monopropellant systems included a 30% improvement in density-specific impulse (Isp) by the year 2000 and subsequent increases every 5 years. The result of this density-Isp goal is a propellant based on HAN that was developed by researchers at the U.S. Air Force Research Laboratory at Edwards Air Force Base, CA, with funding from the U.S. Air Force Office of Scientific Research. Designated AF-M315E (also known by its commercial name ASCENT [Advanced Spacecraft Energetic Non-toxic Propellant]), AF-M315E has a density-Isp improvement of 64% over hydrazine, greater than any other hydrazine replacement yet identified.

The physical property comparison between FLP-106, hydrazine, LMP-103S, and AF-M315E can be found in Table 1. A higher density allows more propellant mass to be stored in the same volume of space, allowing more thrust. Isp is analogous to fuel economy for a car—the higher the Isp, the more thrust per pound of fuel used. There have been many studies on the performance of the propellants, and comparisons have been made between each [16–19]. Compositional differences of LMP-103S and FLP-106 are summarized in Table 2.

Table 1: Physical Properties Between Hydrazine FLP-106, LMP-103S, and AF-M315E [16–19]

FUEL	Isp	DENSITY (g/mL)	COMBUSTION TEMPERATURE (K)
Hydrazine	230	1.0037	1227
FLP-106	255-261	1.357	1910
LMP-103S	244-255	1.238	1873
AF-M315E	257	1.47	2173

Table 2: Compositional Comparison Between FLP-106 and LMP-103S [16–19]

FUEL	H_2O	ADN	AMMONIA	METHANOL	MONOMETHYL-FORMAMIDE
FLP-106	23.90	64.60	—	—	11.50
LMP-103S	13.95	63.00	4.65	18.40	—

CHALLENGES FOR GREEN MONOPROPELLANTS

Despite multiple candidates vying to replace hydrazine, there are still challenges associated with green monopropellant use. Ignition is difficult compared to hydrazine. A study by the German Aerospace Center (DLR) examined thermal ignition of ADN-based monopropellants [20] and found that the water in the ADN-based propellants had to evaporate before decomposition could occur. Two different methods were devised to achieve this objective—one involved thermal ignition with a pilot flame, and the other involved a glow plug insertion. Only the glow plug was found to be successful.

Catalytic ignition of AF-M315E is initiated through a preheated catalyst bed. The catalyst bed requires a large amount of power in order to generate the necessary thermal conditions. Minimizing the necessary heater power while ensuring repeated and consistent ignition over the thruster system's life is critically important and remains an area of active research.

Although the concept of energetic ionic liquids using HAN and ADN is 20 years old, the practical reality of implementing entire propulsion systems around these new fuels is challenging; however, the difficulties are not insurmountable. LMP-103S has already been demonstrated in operational spacecraft, and AF-M315E is currently getting an on-orbit shakedown as part of NASA's Green Propellant Infusion Mission (GPIM).

GPIM REACHES ORBIT

Early on the morning of Tuesday, June 25, 2019, the flames from a SpaceX Falcon Heavy rocket lit up the darkness of Kennedy Space Center

Minimizing the necessary heater power while ensuring repeated and consistent ignition over the thruster system's life is critically important and remains an area of active research.

Launch Complex 39A (Figure 3). The Falcon Heavy hosted the DoD's Space Test Program-2, a multimanifest mission involving DoD, NASA, and National Oceanic and Atmospheric Administration satellites, along with a number of satellites from educational institutions and the private sector [21]. For the spacecraft propulsion community, NASA's GPIM satellite was a particularly important and long-awaited component of the Falcon Heavy launch manifest. Funded by NASA's Technology Demonstration Missions program within the agency's Space Technology Mission Directorate, the satellite was built by Ball Aerospace & Technologies Corp. based on the company's BCP-100 bus Evolved Expendable Launch Vehicle Secondary Payload Adapter-class mission. The GPIM satellite will serve as a testbed for the AF-M315E propellant [22]. The satellite's thrusters were developed by Aerojet Rocketdyne, and the AF-M315E-based propulsion system was codesigned by Ball Aerospace and Aerojet Rocketdyne [23, 24].

Approximately an hour-and-a-half after the successful launch of the Falcon Heavy from Florida with its manifest of 24 satellites, the GPIM satellite deployed from the rocket's second stage and began to power up in anticipation of commands from its ground controllers. Within a week of its launch, controllers fired the satellite's five thrusters in order to test the propulsion subsystem and ensure that GPIM was functioning as designed [21, 26].

Over the next 13 months, the GPIM satellite will perform a number of in-orbit maneuvers, including attitude control, spacecraft pointing, thruster performance characterization and

Figure 3: The SpaceX Falcon Heavy Launch on June 25, 2019 *(Source: Airman 1st Class Zoe Thacker, U.S. Air Force [25]).*

mapping, and orbit lowering, to test the efficacy of the AF-M315E-based propulsion system and demonstrate its viability for future government and commercial spaceflight missions [23].

CONCLUSIONS

Future use of AF-M315E will help lower the cost of spacecraft fueling prior to launch since the fuel is nontoxic and will require fewer safety precautions than the highly-toxic hydrazine propellant currently in use. It will also provide greater flexibility for spacecraft designers due to its high-energy density, which will permit smaller quantities to be used for missions or permit missions to last longer [26]. Green monopropellants are currently being considered for many space missions, including Mars ascent vehicles and hoppers, lunar landers, and deep-space microsatellites [27]. Time will tell whether hydrazine joins "C-Stoff" in the space and rocket propulsion history books. ■

REFERENCES

[1] Schmidt, E. W. "One Hundred Years of Hydrazine Chemistry." Third Conference on Environmental Chemistry of Hydrazine Fuels, September 1987.

[2] Wetmore, D., Maj. "Titan II Blasts Its Way Into History." U.S. Air Force, https://www.af.mil/News/Article-Display/Article/138285/titan-ii-blasts-its-way-into-history/, 24 October 2003.

[3] Iridium. "Hydrazine – Toxic for Humans, but Satellites Love It." https://www.iridium.com/ blog/2017/06/20/ hydrazine-toxic-for-humans-but-satellites-love-it/, 20 June 2017.

[4] Moynihan, P. I. "Back in the Day... Selected Events in Early Monopropellant Hydrazine Thruster Development," 10 July 2006.

[5] Fisher Scientific. "Hydrazine Anhydrous." Material safety data sheet, https://fscimage.fishersci. com/ msds/11040.htm, 29 June 2007.

[6] Stewart, C., Tech Sgt. "Hydrazine Response Team Hones Skills." U.S. Air Force, https://www. 114fw.ang. af.mil/News/114FW-News/Article/863976/hydrazine-response-team-hones-skills/, 20 June 2014.

[7] Martin Marietta Corporation. *Material Compatibility With Space Storable Propellants Design Handbook*, https://ntrs.nasa.gov/archive/nasa/casi.ntrs.nasa. gov/19720019028.pdf, March 1972.

[8] European Parliament and Council. Regulation (EC) No. 1907/2006. "Registration, Evaluation, Authorisation [*sic.*] and Restriction of Chemicals (REACH)," https://eur-lex.europa.eu/legal-content/EN/ TXT/?uri=CELEX:32006R1907, accessed 31 July 2019.

[9] Wingborg, N., C. Eldsäter, and H. Skifs. "Formulation and Characterization of ADN-Based Liquid Monopropellants." Proceedings of the 2nd International Conference on Green Propellants for Space Propulsion (ESA SP-557), Chia Laguna (Cagliari), Sardinia, Italy, edited by A. Wilson, 7–8 June 2004.

[10] University of Applied Sciences Wiener Neustadt. "Final Report Summary – GRASP (Green Advanced Space Propulsion)." https://cordis.europa.eu/project/ rcn/89683/reporting/en, accessed 31 July 2019.

[11] Larsson, A., and N. Wingborg. "Green Propellants Based on Ammonium Dinitramide (ADN), Advances in Spacecraft Technologies." Edited by Dr. Jason Hall, https://www.intechopen.com/ books/advances-in-spacecraft-technologies/green-propellants-based-on-ammonium-dinitramide-adn-, 2011.

[12] Anflo, K., T. A. Grönland, and N. Wingborg. "Development and Testing of ADN-Based Monopropellants in Small Rocket Engines." The 36th AIAA/ASME/SAE/ASEE Joint Propulsion Conference, Huntsville, AL, 16–19 July 2000.

[13] Wilhelm, M., M. Negri, H. Ciezki, and S. Schlechtriem. "Preliminary Tests on Thermal Ignition of ADN-Based Liquid Monopropellants." *Acta Astronautica*, vol. 158, pp. 388–396, https://doi.org/ 10.1016/j.actaastro.2018.05.057, May 2019.

[14] PRISMA (Prototype Research Instruments and Space Mission Technology Advancement). https://earth.esa.int/web/eoportal/satellite-missions/p/prisma-prototype, accessed 31 July 2019.

[15] DeGeorge, D., and S. Fletcher. "The Integrated High Payoff Rocket Propulsion Technology Program (IHPRPT) and Tactical Missile Propulsion Status." Paper presented at the RTO AVT Specialists' Meeting on Advances in Rocket Performance Life and Disposal, Aalborg, Denmark, 23–26 September 2002, https://www.sto.nato.int/publications/STO%20Meeting%20Proceedings/RTO-MP-091/MP-091-02.pdf, accessed 31 July 2019.

[16] Negri, M. "Replacement of Hydrazine: Overview and First Results of the H2020 Project Reform." Paper presented at the 6th European Conference for Aeronautics and Space Sciences (EUCASS), Kraków, Poland, July 2015.

[17] Wurdak, M., F. Strauss, L. Werling, H. K. Ciezki, D. Greuel, R. Lechler, N. Wingborg, D. Hasan, and C. Scharlemann. "Determination of Fluid Properties of the Green Propellant FLP-106 and Related Material and Component Testing With Regard to Applications in Space Missions." Paper presented at the Space Propulsion 2012 Conference, Bordeaux, France, May 2012.

[18] Werling, L. "Experimental Investigations Based on a Demonstrator Unit to Analyze the Combustion Process of a Nitrous Oxide/Ethene Premixed Green Propellant." Paper presented at the 5th CEAS Air & Space Conference, Delft, Netherlands, September 2015.

[19] Spores, A. R., R. Masse, S. Kimbrel, and C. McLean "GPIM AF-M315E Propulsion System." Aerojet Rocketdyne, Redmond, WA, and Ball Aerospace and Technologies Corporation, Boulder, CO, September 2015.

[20] Wilhelm, M., M. Negri, H. Ciezki, and S. Schlechtriem. "Preliminary Tests on Thermal Ignition of ADN-Based Liquid Monopropellants." DLR Institute of Space Propulsion, Hardthausen, Germany, September 2015.

[21] Skelly, C., and K. Fox. "NASA Technology Missions Launch on SpaceX Falcon Heavy." https://www.nasa.gov/press-release/nasa-technology-missions-launch-on-spacex-falcon-heavy, accessed 1 August 2019.

[22] U.S. Air Force Office of Scientific Research. "Long Awaited Launch of NASA's GPIM Mission to Use AFRL-Developed Propellant." https://www.wpafb.af.mil/News/Article-Display/Article/1891179/ long-awaited-launch-of-nasas-gpim-mission-to-use-afrl-developed-propellant/, accessed 1 August 2019.

[23] NASA. "Green Propellant Infusion Mission." https://www.nasa.gov/sites/default/files/atoms/ files/g-484591_gpim_factsheet.pdf, accessed 1 August 2019.

[24] Mohon, L. (editor). "Green Propellant Infusion Mission (GPIM) Overview." https://www.nasa.gov/ mission_pages/tdm/green/overview.html, accessed 1 August 2019.

[25] Thacker, Z., Airman 1st Class. "45th SW Support Falcon Heavy STP-2 Rocket Launch." U.S. Air Force, https://www.patrick.af.mil/News/Photos/igphoto/2002149671/, accessed 30 July 2019.

[26] Hall, L. (editor). "Green Propellant Infusion Mission Fires Thrusters for the First Time." https://www.nasa.gov/directorates/spacetech/home/tdm/gpim_fires_thrusters_for_first_time, accessed 1 August 2019.

[27] Deans, C. M., et. al. "An Evaluation of the Impacts of AF-M315E Propulsion Systems for Varied Mission Applications." NASA Glenn Research Center, https://ntrs.nasa.gov/archive/nasa/ casi.ntrs.nasa.gov/20150021510.pdf, accessed 31 July 2019.

BIOGRAPHIES

NICHOLAS KEIM is the Deputy Director of the Johns Hopkins University (JHU) Whiting School of Engineering's Energetics Research Group (ERG) and principal investigator at the Advanced Engine and Rocket (AERo) Fuels Laboratory. He has worked at the Chemical Propulsion Information Analysis Center and performed original research on rocket propellants and propulsion topics, resulting in the publication of over 40 technical papers. In 2012, he helped establish the AERo Fuels Laboratory, which is dedicated to the scientific investigation of rocket and aerospace fuels for space launch and hypersonic applications. Mr. Keim holds a B.S. in mechanical engineering from JHU and an M.S. in mechanical engineering from Imperial College London.

ALEXANDER BISHOP is an associate staff engineering supporting propellant and fuel-related researcher at the JHU Whiting School of Engineering's ERG. He serves as the technical representative to the Joint Army Navy NASA Air Force (JANNAF) Interagency Propulsion Committee's Air Breathing Propulsion, Space Propulsion, and Modeling and Simulation subcommittees. His current fuel research topic areas include RP-2 and methane/LNG for space launch vehicles, green monopropellants for space craft propulsion, and endothermic fuels for hypersonic vehicles. Mr. Bishop holds a chemical engineering degree from the University of Maryland Baltimore County and is pursuing a master's degree in chemical and biomolecular engineering from JHU.

BENJAMIN HILL-LAM is an associate staff engineer involved in studying hydrocarbon fuels' thermal stability performance at the JHU Whiting School of Engineering's ERG. He currently works on research to develop a standardized thermal stability metric utilizing the Compact Rapid Assessment of Fuel Thermal Integrity rig in the Advanced Engine and Rocket Fuels lab. His other research areas include endothermic fuels research for hypersonic vehicles and green propellant materials compatibility. He serves as the Energetic Research Group's technical representative for the JANNAF Liquid Propulsion and Combustion subcommittees. Mr. Hill-Lam holds a bachelor's degree in physics from Bowdoin College and is currently pursuing a master's degree in materials science and engineering at JHU.

BENJAMIN SCHWANTES is the Managing Editor of the JANNAF (Joint Army Navy NASA Air Force) *Journal of Propulsion and Energetics* published by the ERG at the JHU Whiting School of Engineering. Prior to joining ERG, he served as a research associate at the German Historical Institute in Washington, DC, where he helped to manage a long-term, online research and publication project on immigration and entrepreneurship. He has served as editor and reviewer for various publications and journals and authored articles on entrepreneurship, ethnicity, business, and communication for immigrant entrepreneurship. Dr. Schwantes received his B.A. in history from the University of Pittsburgh and his M.A. and Ph.D. in the history of technology and industrialization from the University of Delaware.

CONFERENCES AND SYMPOSIA

DARPA Launch Challenge (DLC)
16 April 2018 to 31 December 2019
http://www.darpalaunchchallenge.org ▸

NOVEMBER 2019

ISR & C2 Battle Management U.S. Conference
5–7 November 2019
Crowne Plaza
Old Town Alexandria, VA
https://isrusa.iqpc.com ▸

2019 Sensors & Seekers Test Technology Working Group (SSTT WG) Annual Workshop
5–6 November 2019
AEgis Technologies
Huntsville, AL
https://www.dsiac.org/events/2019-sensors-seekers-test-technology-working-group-sstt-wg-annual-workshop ▸

DECEMBER 2019

2019 Defense Manufacturing Conference (DMC)
2–5 December 2019
Phoenix Convention Center
Phoenix, AZ
http://www.dmcmeeting.com ▸

Aircraft Structural Integrity Program (ASIP) Conference
2–5 December 2019
San Antonio, TX
http://www.asipcon.com ▸

2019 IEEE International Conference on Artificial Intelligence and Virtual Reality (AIVR)
9–11 December 2019
San Diego, CA
https://conferences.ieee.org/conferences_events/conferences/conferencedetails/46125 ▸

Military Standard 810H (MIL-STD-810H) Testing NTS (Winter 2019)
9–12 December 2019
Huntsville, AL
https://equipment-reliability.com/training-calendar/nts-huntsville-al-dec9-12 ▸

JANUARY 2020

AIAA SciTech Forum 2020
6–10 January 2020
Hyatt Regency
Orlando, FL
https://www.aiaa.org/scitech ▸

2020 IEEE/SICE International Symposium on System Integration (SII)
13–15 January 2020
Honolulu, HI
https://conferences.ieee.org ▸ conferences_events/conferences/conferencedetails/46433 ▸

Transformative Vertical Flight 2020
21–23 January 2020
Doubletree Hilton
San Jose, CA
https://vtol.org/events/transformative-vertical-flight-2020 ▸

44th International Conference and Expo on Advanced Ceramics and Composites (ICACC 2020)
26–31 January 2020
Hilton Daytona Beach Oceanfront Resort
Daytona Beach, FL
https://ceramics.org/event/44th-international-conference-and-expo-on-advanced-ceramics-and-composites ▸

66th Annual Reliability & Maintainability Symposium (RAMS)
27–30 January 2020
Palm Springs, CA
http://www.rams.org/ ▸

FEBRUARY 2020

2020 High Temple Workshop
3–6 February 2020
Hilton Sedona Resort at Bell Rock
Sedona, AZ
https://hightemple.udri.udayton.edu ▸

Fundamentals of Random Vibration and Shock Testing Course (California)
10–12 February 2020
Westpak Laboratory, San Jose, CA
https://equipment-reliability.com/training-calendar/vibration-and-shock-testingfebruary-10-12-2020 ▸

2020 Air Warfare Symposium
26–28 February 2020
Orlando, FL
https://www.afa.org/events/calendar/2020-02-26/air-warfare-symposium ▸

MARCH 2020

2020 IEEE Aerospace Conference
7–14 March 2020
Yellowstone Conference Center
Big Sky, MO
https://aeroconf.org ▸

2020 Annual Directed Energy Science and Technology Symposium
9–13 March 2020
West Point, NY
https://protected.networkshosting.com/depsor/DEPSpages/events.html ▸

23rd AIAA International Space Planes and Hypersonic Systems and Technologies Conference
10–12 March 2020
Montréal, Québec, Canada
https://www.aiaa.org/home/events-learning/event/2020/03/10/default-calendar/23rd-aiaa-international-space-planes-and-hypersonic-systems-and-technologies-conference ▸

For more events, visit:
dsiac.org/events/upcoming-events ▸

DSIAC

Defense Systems
Information Analysis Center

4695 Millennium Drive
Belcamp, MD 21017-1505

DSIAC ONLINE

www.dsiac.org

DSIAC PRODUCTS AND SERVICES INCLUDE:

- Performing literature searches.
- Providing requested documents.
- Answering technical questions.
- Providing referrals to subject matter experts (SMEs).
- Collecting, electronically cataloging, preserving, and disseminating Defense Systems scientific and technical information (STI) to qualified users.
- Developing and deploying products, tools, and training based on the needs of the Defense Systems community.
- Fostering and supporting the DSIAC technical Communities of Practice.
- Participating in key DoD conferences and forums to engage and network with the S&T community.
- Performing customer-funded Core Analysis Tasks (CATs) under pre-competed IDIQ Delivery Orders.

DSIAC SCOPE AREAS INCLUDE:

- Advanced Materials
- Autonomous Systems
- Directed Energy
- Energetics
- Military Sensing
- Non-Lethal Weapons
- Reliability, Maintainability, Quality, Supportability, and Interoperability (RMQSI)
- Survivability and Vulnerability
- Weapon Systems

CONNECT WITH US ON SOCIAL MEDIA!